

3DID: Direct 3D Inverse Design for Aerodynamics with Physics-Aware Optimization

Yuze Hao¹, Linchao Zhu^{1,2}, Yi Yang^{1,2*}

¹ College of Computer Science and Technology, Zhejiang University

² The State Key Lab of Brain-Machine Intelligence, Zhejiang University

Abstract

Inverse design aims to design the input variables of a physical system to optimize a specified objective function, typically formulated as a search or optimization problem. However, in 3D domains, the design space grows exponentially, rendering exhaustive grid-based searches infeasible. Recent advances in deep learning have accelerated inverse design by providing powerful generative priors and differentiable surrogate models. Nevertheless, current methods tend to approximate the 3D design space using 2D projections or fine-tune existing 3D shapes. These approaches sacrifice volumetric detail and constrain design exploration, preventing true 3D design from scratch. In this paper, we propose a **3D Inverse Design (3DID)** framework that directly navigates the 3D design space by coupling a continuous latent representation with a physics-aware optimization strategy. We first learn a unified physics–geometry embedding that compactly captures shape and physical field data in a continuous latent space. Then, we introduce a two-stage strategy to perform physics-aware optimization. In the first stage, a gradient-guided diffusion sampler explores the global latent manifold. In the second stage, an objective-driven, topology-preserving refinement further sculpts each candidate toward the target objective. This enables **3DID** to generate high-fidelity 3D geometries, outperforming existing methods in both solution quality and design versatility.

1 Introduction

Inverse design seeks to identify the initial variables of a physical system that, under given constraints, optimizes a specified objective function. This fundamental challenge occurs across many scientific and engineering disciplines, such as materials science, mechanical engineering, aerospace design, and supports applications ranging from automotive body shaping [1] and nano-photonic device engineering [2] to mechanical materials design [3, 4] and physics detector development [5].

Despite its broad impact, efficiently exploring the design space toward a target objective presents significant challenges. First, inverse design must contend with the inherent complexity of simulating physical systems for evaluation. These simulations are often nonlinear and high-dimensional, requiring fine discretizations that dominate computational resources [6, 7]. Second, the design landscape is extremely large, inherently nonconvex, and riddled with local minima, making exhaustive global search infeasible [8, 9]. In 3D domains, where inverse design usually involves direct geometry optimization, the number of degrees of freedom grows exponentially [10]. This rapid growth in geometric complexity drives up simulation expense and intensifies the search challenge.

To tackle inverse design in the 3D domain, various techniques have been proposed [1, 11, 12], yet they fall short of addressing the above challenges. Traditional approaches such as adjoint-based gradient methods [13, 14, 15] and Bayesian optimization [16, 17] provide broad applicability but depend on

*Corresponding author.

repeated high-fidelity simulations that incur prohibitive computational cost. With recent advances in deep learning, pretrained surrogate models [18, 19, 20, 21] can efficiently approximate the forward physical process and support end-to-end backpropagation to update design variables, speeding up convergence by orders of magnitude. However, many prior methods adopt two simplifications. One replaces the 3D design with 2D proxies [1, 11] (multi-view renderings or silhouettes), which removes geometry information. The other requires an initial geometry as the starting point for subsequent refinement [22, 23, 24]. In practice, both assumptions restrict design exploration and hinder a thorough search of complex 3D design spaces (see Fig. 1). As a result, they cannot support the full exploration of complex three-dimensional design spaces, limiting coverage to a narrow subset of feasible geometries.

We identify two primary challenges in 3D inverse design. 1) The high dimensionality of 3D physics-geometry-coupled spaces impedes exploration. Inverse design must simultaneously optimize geometric structures while accurately evaluating their resulting physical properties. This coupling, combined with the continuous high-resolution nature of both shape and physical fields, makes the direct 3D exploration extraordinarily difficult. 2) The lack of optimization strategies that balance the exploration–validity trade-off. Refining a baseline geometry with a surrogate model ensures constraint compliance and design validity, but it confines the search to a local neighborhood and can introduce adversarial artifacts when driven too far [25, 26]. On the other hand, sampling candidates with a generative model offers broader exploration yet leaves results vulnerable to biases in the training data [27]. Consequently, samples stay tethered to the prior and tend to imitate prevalent patterns rather than pushing toward novel optima.

To address these challenges, we introduce **3DID**, a 3D inverse-design framework that explores the design space without relying on simplified parameterizations or predefined shapes. Rather than directly searching the prohibitively large, continuous physics-geometry-coupled space, we first learn a continuous physics–geometry unified latent representation. This compact embedding preserves fine-grained shape and physical field variations while dramatically reducing both dimensionality and computational cost, thereby overcoming the dual obstacles of large-scale shape optimization and physics-aware simulation. Building on this latent space, we then deploy a two-stage optimization pipeline to tackle the exploration–validity trade-off. It begins with a gradient-guided diffusion sampler that traverses the manifold from pure noise to generate diverse, physics-informed candidates by steering sampling toward high-performance regions using objective gradients. Each candidate then undergoes topology-preserving optimization, which further improves objective performance under strict mesh-quality and connectivity constraints, ensuring geometric integrity and preventing adversarial artifacts. Together, these components enable 3DID to discover novel, high-fidelity 3D designs that reliably meet target objectives. In summary, our contributions are threefold:

- (1) We propose a continuous latent embedding that jointly encodes detailed 3D geometry and high-fidelity physical fields, enabling an efficient, unified search within a compact latent manifold.
- (2) We develop a two-stage optimization pipeline that begins with gradient-guided diffusion sampling for global exploration and followed by topology-preserving refinement, optimizing each candidate toward the desired objective while strictly maintaining structural integrity.

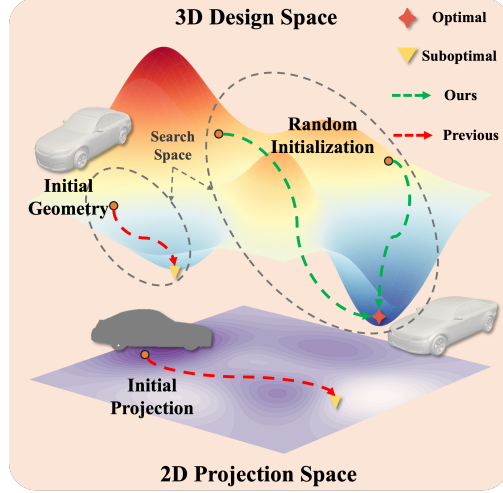


Figure 1: **Motivation of 3DID.** Existing 3D inverse-design methods either rely on reduced-dimensional representations (2D projections or fixed parameterizations) that constrain design freedom, or require an initial geometry as a starting point for local refinement, which highly constrains the search space. In contrast, 3DID overcomes these limitations by directly exploring the full 3D design space from random initialization.

(3) We validate our 3DID framework on aerodynamic shape optimization, demonstrating that it consistently generates novel geometries whose superior performance is confirmed through surrogate evaluations and high-fidelity CFD simulations, significantly surpassing baseline methods.

2 Related work

2.1 Inverse Design

Compared with the forward PDE problem, which predicts the physical response of a given design using numerical solvers or learned surrogates [28, 29, 30, 31, 32, 33], inverse design seeks the design variables that achieve a target objective under engineering constraints [26, 18, 34]. Inverse design is a fundamental problem in many domains of science and engineering disciplines, including mechanical engineering [35, 36], material science [37, 38, 39], chemical engineering [40], medical engineering [41], and aerospace engineering [22, 6, 42]. Classical approaches typically combine high fidelity physics solvers with sampling-based optimization methods such as the Cross Entropy Method [43] or Gaussian-process model with Bayesian optimization [44] to explore the design space. With the advent of differentiable simulators, inverse design can be posed directly as a gradient-based optimization problem [41, 45]. More recently, deep learning driven methods have shown great promise by learning surrogate models that approximate forward physics and allow end-to-end backpropagation [18, 19]. Furthermore, generative models, including variational autoencoders [46], GAN [47, 48] and diffusion models [26, 49] have been applied to inverse design. While prior methods mainly excel in 2D or low-dimensional settings, we propose a framework that directly navigates the full 3D design space via physics-aware optimization.

2.2 Aerodynamic Shape Optimization

Aerodynamic shape optimization is a classical inverse design task that seeks geometries minimizing drag while satisfying constraints on lift, stability, and other performance criteria [50, 51, 52, 53]. Generally, effective optimization critically depends on two key components: shape representation and optimization strategy. Traditional approaches typically employ simplified, low-dimensional representations such as 2D projections [11, 54, 1] or spline-based parameterizations [55, 56, 57] to reduce dimensionality and computational costs. Optimization is then performed using gradient-based adjoint solvers for efficient local refinement [24, 58, 59]. Additionally, to accelerate convergence, many methods optimize from a pre-selected baseline geometry [22, 23, 24]. In contrast, we propose a guided diffusion model over a latent shape representation, enabling the design of unconstrained 3D geometries directly from noise, without relying on initial shapes or 2D profiles.

3 Methods

In this section, we first formalize the 3D inverse design problem (Section 3.1). We then introduce our physics–geometry unified representation (Section 3.2), describe the gradient-guided diffusion sampling process (Section 3.3), and detail the topology-preserving refinement stage (Section 3.4). Finally, we provide our implementation details (Section 3.5).

3.1 Problem Formulation

We consider the problem of 3D inverse design, where the goal is to identify a solid input geometry \mathbf{M} for a physical system that optimizes specified performance objectives while satisfying geometric constraints. Formally, let $\mathbf{M} \subset \mathbb{R}^3$ denote a solid geometry, and let $\mathcal{F}(\mathbf{M})$ be the corresponding steady-state physical field (e.g., pressure or temperature distribution) governed by a partial differential equation (PDE) or an ordinary differential equation (ODE). We define the design objective as:

$$\mathcal{J}(\mathbf{M}) := \mathcal{J}(\mathbf{M}, \mathcal{F}(\mathbf{M})), \quad (1)$$

which may measure quantities such as drag, lift, and structural compliance. Specifically, \mathcal{J} depends on \mathbf{M} in two ways: implicitly, via the resulting physical field $\mathcal{F}(\mathbf{M})$ on which \mathcal{J} is evaluated, and explicitly, via direct geometric properties defined on \mathbf{M} . The classical inverse design aims to solve:

$$\begin{aligned} \mathbf{M}^* &= \arg \min_{\mathbf{M}} \mathcal{J}(\mathbf{M}, \mathcal{F}(\mathbf{M})) \\ \text{s.t. } \mathbf{C}(\mathbf{M}, \mathcal{F}(\mathbf{M})) &\leq \mathbf{0}, \end{aligned} \quad (2)$$

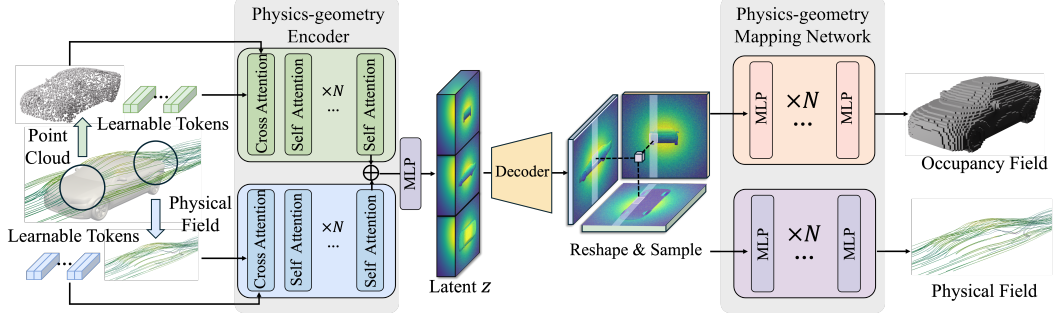


Figure 2: **The overview of PG-VAE.** We use transformers to encode the design geometry and its associated physical field, along with learnable tokens, into a compact triplane latent representation z . A decoder then upsamples the latent z into high-resolution triplane feature maps, which can be reshaped into three orthogonal planes. Finally, a physics–geometry mapping network is applied to reconstruct both the occupancy field and the corresponding physical field from these feature maps.

where the solution M^* is the geometry that minimizes the performance objective, C aggregates design constraints, such as volume, manufacturability, and boundary conditions.

3.2 Physics-Geometry Unified Representation

To compactly encode 3D geometry and its physical field, we adopt a triplane representation learned via our Physics-Geometry VAE (PG-VAE). As shown in Figure 2, it includes: (1) A *physics–geometry encoder* that maps input geometry and physical field into a latent code. (2) A *latent-to-triplane decoder* that reconstructs triplane feature maps from the latent code. (3) A *physics–geometry mapping network* that recovers the 3D geometry and physical field from the triplane.

Physics-Geometry Encoder. The physics–geometry encoder comprises two parallel branches: one for processing raw 3D geometry, and the other for encoding the associated physical field. Inspired by [60], each branch uses learnable tokens to capture both local and global context. For the geometry branch, given uniformly sampled point clouds $P_{geo} \in \mathbb{R}^{N_g \times C_g}$ from the geometry, where N_g is the number of points and C_g represents features including normalized positions and surface normals, we utilize Fourier features [61] to encode positional structure. Then, a set of learnable tokens $e_g \in \mathbb{R}^{(3 \times r \times r) \times d_e}$ queries information from these points via cross-attention and self-attention layers, resulting in geometry latent tokens $z_g \in \mathbb{R}^{(3 \times r \times r) \times d_z}$. The physical-field branch follows the same structure, processing uniformly sampled physical-field points $P_{phy} \in \mathbb{R}^{N_p \times C_p}$, where N_p is the number of points and C_p is the dimension of physical-field features. Learnable tokens $e_p \in \mathbb{R}^{(3 \times r \times r) \times d_e}$ undergo similar attention layers to produce physical-field latents $z_p \in \mathbb{R}^{(3 \times r \times r) \times d_z}$. Finally, geometry and physical tokens are concatenated and passed through MLP layers to form the unified latent representation $z = \text{MLP}(\text{Concat}(z_g, z_p))$, where $z \in \mathbb{R}^{(3 \times r \times r) \times d_z}$.

Latent-to-Triplane Decoder. After obtaining the unified physics–geometry latent representation, we apply a decoder to formulate the triplane representation. Prior to decoding, we reshape the latent tokens by vertically concatenating three planes, yielding the reshaped latent tensor $z \in \mathbb{R}^{r \times (3 \times r) \times d_z}$, following [62]. Subsequently, the latent tensor is passed through a series of convolutional layers for upsampling. The output is then reshaped into the final triplane features $T_{xy}, T_{xz}, T_{yz} \in \mathbb{R}^{R \times R \times d_t}$, where R denotes the resolution of each plane and d_t is the feature dimension per pixel.

Physics-Geometry Mapping Network. The mapping network serves to reconstruct 3D geometry and the associated physical field from the learned triplane representation. We utilize two parallel MLP branches: one for predicting geometric occupancy and one for estimating the physical field. Given a query point $q \in \mathbb{R}^3$, we project it onto the three orthogonal planes and extract features. The aggregated feature is computed as $t_q = T_{xy}(q_{xy}) + T_{xz}(q_{xz}) + T_{yz}(q_{yz})$, where q_{xy}, q_{xz}, q_{yz} denote the 2D projections of q onto the respective planes. The aggregated feature t_q is then fed into the MLP branches to predict the occupancy field and physical field values at the corresponding point q .

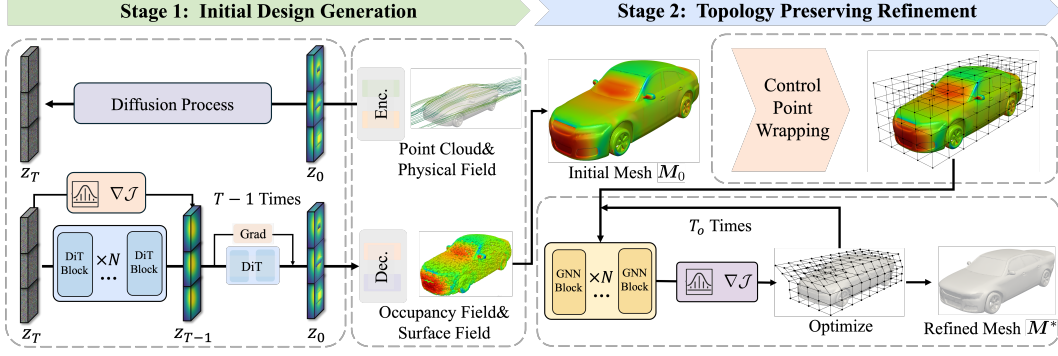


Figure 3: **The optimization framework of 3DID.** Starting from noise, we guide diffusion using objective gradients to steer the latent toward high-performance regions. The decoded triplane then yields an initial mesh M_0 and its surface physical field φ , which is then refined via backpropagation over a free-form deformation lattice to improve performance while preserving topology.

End-to-End Training. Our VAE model is trained end-to-end to jointly reconstruct 3D geometry and the associated physical field. For occupancy field reconstruction, we employ the Binary Cross-Entropy (BCE) loss \mathcal{L}_{BCE} to supervise the predicted occupancy. To reconstruct the physical field, we utilize the Mean Squared Error (MSE) loss \mathcal{L}_{MSE} . Additionally, we incorporate a KL divergence loss \mathcal{L}_{KL} to regularize the latent space. Overall, our training loss can be formulated as:

$$\mathcal{L}_{\text{PG-VAE}} = \lambda_{\text{BCE}} \mathcal{L}_{\text{BCE}} + \lambda_{\text{MSE}} \mathcal{L}_{\text{MSE}} + \lambda_{\text{KL}} \mathcal{L}_{\text{KL}}, \quad (3)$$

where $\lambda_{\text{BCE}}, \lambda_{\text{MSE}}, \lambda_{\text{KL}}$ are weighting coefficients.

3.3 Objective Guided Diffusion

Once the PG-VAE is trained, it provides a compact, expressive latent code z that jointly captures 3D geometry and its physical field. We then train a diffusion model [63, 64] on these latents, enabling direct generation of samples on the learned manifold from pure noise. To drive inverse design, we inject gradients of the task objective \mathcal{J} into the diffusion sampling, as shown in Figure 3.

In standard diffusion sampling, each denoising step predicts noise via the learned score function:

$$\epsilon_{\phi}(z_t, t) = -\sqrt{1 - \alpha_t} \nabla_{z_t} \log p(z_t), \quad (4)$$

where $\nabla_{z_t} \log p(z_t)$ denotes the score function, *i.e.*, the gradient of the log-probability density of the latent variable z_t . By iteratively denoising, the model guides samples toward high-probability regions of the data manifold. In our case, we need to consider not only guiding the noise towards the feasible data manifold, but we also need to incorporate optimization of \mathcal{J} during the sampling. Therefore, inspired by [65, 66], we replace the unconditional score with the conditional score $\nabla_{z_t} \log p(z_t | \mathcal{J})$. By Bayes' rule, we can derive:

$$\nabla_{z_t} \log p(z_t | \mathcal{J}) \propto \nabla_{z_t} \log p(z_t) + \nabla_{z_t} \log p(\mathcal{J} | z_t). \quad (5)$$

Here, $\nabla_{z_t} \log p(z_t)$ corresponds to the standard score function learned by the diffusion model, while $\nabla_{z_t} \log p(\mathcal{J} | z_t)$ acts as an additional guidance term that incorporates the influence of the design objective. Since $\nabla_{z_t} \log p(\mathcal{J} | z_t)$ is unknown, we approximate it by:

$$\nabla_{z_t} \log p(\mathcal{J} | z_t) \simeq \nabla_{z_t} \log p(\mathcal{J} | \hat{z}_0(z_t)) \propto -\nabla_{z_t} \mathcal{J}(\hat{z}_0(z_t)), \quad (6)$$

where $\hat{z}_0(z_t)$ denotes the estimate of the clean latent code given the noisy latent z_t , following [66]. Accordingly, we adjust the predicted noise to incorporate the influence of the design objective \mathcal{J} , resulting in the guided noise prediction:

$$\epsilon'_{\phi}(z_t, t) = \epsilon_{\phi}(z_t, t) + \gamma \nabla_{z_t} \mathcal{J}, \quad (7)$$

where ϵ'_{ϕ} is the modified noise prediction, and γ is a scaling coefficient that controls the strength of the guidance. This objective-aware adjustment steers the sampling trajectory toward latent regions that both conform to the learned data distribution and advance the target design objective \mathcal{J} .

3.4 Topology-Preserving Refinement

After objective-guided diffusion, we obtain an optimized latent code z^* , which is reshaped into triplane feature maps and decoded by the physics–geometry mapping network to generate an initial 3D mesh M_0 with vertex set $V_0 = \{v_j\}_{j=1}^N$ and its associated physical field $\varphi = \{\varphi_j\}_{j=1}^N$, as shown in Figure 3. Although guided by the design objective, the generated designs remain highly biased by the prior distribution of designs from the training data [27]. We introduce a topology-preserving refinement stage based on free-form deformation (FFD) [67, 68], controlled by gradient descent.

Specifically, we first wrap M_0 in a 3D lattice of control points $C = \{c_i\}_{i=1}^K$. These control points form a flexible control grid that allows smooth and structured adjustment of the mesh shape while preserving its topology. The deformation of each vertex v_j is computed as:

$$v'_j(C) = \sum_{i=1}^K \mathcal{B}_i(v_j) c_i, \quad (8)$$

where $\mathcal{B}_i(v_j)$ denotes the i -th trivariate Bernstein basis function [68] evaluated at the normalized parametric coordinate of vertex v_j . These basis functions provide smooth, localized influence from the control points, enabling flexible yet coherent deformation across the mesh.

At the beginning of the refinement process, the control points are unmodified, so $v'_j(C) = v_j$. The initial vertex–field pairs $\{(v'_j(C), \varphi_j)\}$ are then fed into a pretrained GNN surrogate f_{GNN} which estimates the current design objective based on the mesh geometry and physical attributes:

$$\hat{\mathcal{J}}(C) = f_{\text{GNN}}\left((v'_j(C), \varphi_j)_{j=1}^N\right). \quad (9)$$

With this differentiable surrogate model, we optimize the control points to improve the design objective. The overall refinement loss is defined as:

$$\mathcal{L}(C) = \hat{\mathcal{J}}(C) + \lambda_{\text{smooth}} \sum_{i=1}^K \|\Delta c_i\|^2 + \lambda_{\text{vol}} \sum_{\text{cells}} \left(\frac{V_{\text{def}}}{V_{\text{orig}}} - 1\right)^2, \quad (10)$$

where Δc_i are control-point displacements, and the term weighted by λ_{smooth} penalizes large displacements for smooth deformations, while the term weighted by λ_{vol} penalizes cell-wise volume changes to ensure geometric consistency. Control points are updated via:

$$C^{(t+1)} = C^{(t)} - \eta \nabla_C \mathcal{L}(C^{(t)}), \quad (11)$$

We optimize using AdamW with a cosine-annealed learning rate η . Iteration continues until an iteration count T_o is reached. The resulting vertices $V^* = \{v_j^*\}$, obtained via the FFD mapping (Eq. 8), define the refined mesh M^* , which preserves topology and improves target performance.

3.5 Implementation Details

To train our PG-VAE, we sample $N_g = N_p = 50,000$ points as input and use the physics–geometry encoder with one cross-attention layer and 8 self-attention layers with 12 heads and $d_z = 64$, plus $r = 64$ learnable tokens of dimension $d_e = 768$, yielding a latent code of $d_z = 32$. The decoder upsamples via one self-attention layer and five ResNet blocks [69] to a triplane with $R = 256$ and channel $d_t = 64$. Each branch’s mapping network has five linear layers with a hidden dimension of 32. We train the VAE model with loss weights $\lambda_{\text{BCE}} = 10^{-3}$, $\lambda_{\text{MSE}} = 10^{-5}$, $\lambda_{\text{KL}} = 10^{-6}$. During training, we sample 50,000 points from the unit domain to supervise both occupancy and physical-field predictions. For occupancy, we adopt the semi-continuous formulation following [60]. We use a learning rate of $1e-4$, a batch size of 8 per GPU, and train for 100K steps. For the diffusion model, we employ 10 layers of DiT blocks [70], each with 16 attention heads of dimension 72. We train the diffusion model with 1000 denoising steps. For objective-guided sampling, an auxiliary U-Net surrogate predicts the task objective directly in latent code z . To train the diffusion model, we use a learning rate of $5e-5$, a batch size of 4 per GPU, and train for 300K. In topology-preserving refinement, we deform candidates via a $20 \times 6 \times 6$ control-point grid along the x, y, and z axes. For the surrogate model f_{GNN} , we adopt MeshGraphNet [30] as our surrogate given its strong performance in mesh-based physical simulations. The surrogate is trained to predict aerodynamic drag from paired samples of geometry and ground-truth physical fields collected from the dataset. The model is trained with a learning rate of $1e-5$, a batch size of 8 per GPU, and trained for 100K. All models are trained with AdamW optimizer [71]. More training details of 3DID are included in the Appendix.

Table 1: **Quantitative comparison for aerodynamic vehicle design.** The confidence interval information is detailed in the Appendix. Note that our method shows a slight drop in coverage, mainly because the topology-preserving refinement pushes designs beyond the original distribution to achieve better aerodynamic performance.

Method	Pred-Drag↓	Sim-Drag↓	Novelty↑	Coverage↑
GP, Voxel	0.2997	0.4254	1.0399	0.5200
GP, Voxel+PCA	0.3059	0.4363	0.9734	0.5850
CEM, Voxel	0.2951	0.4097	0.9792	0.4350
CEM, Voxel+PCA	0.3088	0.4393	0.9864	0.5100
CEM, TripNet	0.3154	0.4161	1.0399	0.6050
Backprop, Voxel	0.2979	0.4146	0.9860	0.4750
Backprop, Voxel+PCA	0.3061	0.4614	0.9798	0.4950
Backprop, TripNet	0.3153	0.4170	1.0294	0.5900
3DID–NoTopoRefine (ours)	0.2623	0.3766	0.9195	0.6950
3DID (ours)	0.2607	0.3536	1.1709	0.4300

4 Experiments

In the experiments, we aim to answer the following questions: (1) Does 3DID outperform traditional, sampling-based, and backpropagation methods in finding high-quality designs? (2) Does our unified physics–geometry triplane representation yield better objectives than alternative latent or purely geometric embeddings? (3) Does our two-stage pipeline outperform single-stage diffusion sampling and other standard optimization methods? To answer these questions, we evaluate our method on the vehicle aerodynamic shape optimization task, a representative example of 3D inverse design.

In the following sections, we first introduce our dataset and evaluation metrics (Section 4.1). Next, we describe our experimental setup and compare against baseline methods (Section 4.2). Finally, we present two ablation studies: one on the unified physics-geometry representation (Section 4.3) and one on the two-stage optimization strategy (Section 4.4).

4.1 Dataset and Evaluation Details

Dataset. We conduct our experiments on the DrivAerNet++ dataset [72, 73], the largest available collection for aerodynamic car design, comprising over 8,000 diverse geometries paired with high-fidelity CFD simulations. For training, we use the entire dataset. We first normalize each geometry to fit within a unit cube and apply the same scaling to the simulation fields. We then uniformly sample surface point clouds with corresponding normals from the geometry. Finally, for both the occupancy field and the physical field, we adopt the data extraction strategy of Park *et al.* [74], using a grid resolution of 256. Further details of our data preparation are given in the Appendix.

Evaluation Metrics. We evaluate 3DID using four metrics. **Pred-Drag** is the drag coefficient estimated by a trained surrogate model, offering an approximation of the design objective. **Sim-Drag** is the drag coefficient obtained via high-fidelity CFD simulation, delivering an unbiased evaluation of aerodynamic performance. **Novelty** computes the average nearest neighbor distance from each generated design to its closest training example, indicating how distinct the designs are from existing ones. **Coverage** captures how well the generated designs cover the training distribution by measuring, for each training sample, the distance to its nearest generated design (using a k-nearest neighbor lookup) and reporting the fraction of training examples that fall within a predefined threshold. To extract features from the generated geometries, we use the pretrained PointNet model from [75]. Detailed evaluation procedures and simulation parameters are provided in the Appendix.

4.2 3D Vehicle Aerodynamic Design

In this experiment, we evaluate each inverse-design method on the aerodynamic shape optimization task, where the objective \mathcal{J} is to reduce the drag force of the designed vehicles. All methods are trained on the same collection of car geometries paired with high-fidelity CFD simulations. As baselines, we compare against the Cross-Entropy Method (CEM) [43], the Gaussian-process surrogate with

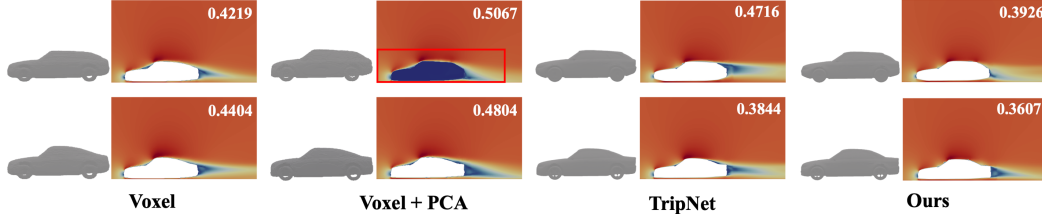


Figure 4: **Qualitative comparisons of different representations.** Each row shows four candidates with geometry (left) and simulated velocity field (right) with Sim-Drag in the top-right. Despite equal resolution, voxel methods incur higher drag and often yield non-watertight shapes (red box) due to coarse discretization. Our continuous latent representation produces watertight, smooth designs with superior aerodynamic performance, outperforming both voxel-based and geometry-only approaches.

Table 2: **Ablation study on representation choices.**

Method	Pred-Drag↓	Sim-Drag↓	Novelty↑	Coverage↑
Voxel	0.2722	0.4318	1.0683	0.3450
Voxel+PCA	0.2720	0.4565	0.9858	0.5750
TripNet	0.2698	0.4066	1.0580	0.5500
3DID-NoTopoRefine (ours)	0.2623	0.3766	0.9195	0.6950
3DID (ours)	0.2607	0.3536	1.1709	0.4300

Bayesian optimization(GP) [44], and the gradient-based backpropagation method(Backprop) [18]. To evaluate the impact of 3D encoding, the optimizer is instantiated with three representations: a dense voxel grid [76], a PCA-compressed voxel grid (Voxel+PCA) [22], and a pure geometry triplane network (TripNet) [21]. GP with the triplane representation is omitted due to its high computational cost. For fairness, we generate 64 candidate designs per method and report the average performance in Table 1. Architectures of baselines and training details are provided in the Appendix.

From Table 1, it can be observed that 3DID delivers the best drag force result for both pred-drag and sim-drag compared to all baselines. Specifically, our full 3DID model reduces simulated drag by 13.6% relative to the strongest baseline. These results demonstrate the effectiveness of our pipeline in discovering high-performance designs. Furthermore, our method achieves the highest novelty score (1.1709), indicating its ability to explore diverse design variations. Note that the drop in coverage occurs because topology-preserving refinement pushes designs beyond the training distribution to boost aerodynamic performance. A detailed ablation on the cascade optimization strategy is presented in Section 4.4. More visualization results and evaluation are presented in the Appendix.

4.3 Ablation Study on Physics–Geometry Unified Representation

In this experiment, we evaluate the performance with different representations, including Voxel [76], Voxel with PCA [22] and the pure geometry triplane (TripNet) [21]. For Voxel and Voxel with PCA, we first train a variational autoencoder (VAE) to embed the raw data into a compact latent space and then learn a diffusion model within that space. Finally, we employ our two-stage optimization pipeline consisting of gradient-guided diffusion sampling followed by topology-preserving refinement to generate diverse design candidates. Because the baseline representations do not include physical field information, we retrain a surrogate graph neural network that takes only geometry as input for the refinement stage. The results are reported in Table 2.

As shown in Table 2, our 3DID method outperforms all baselines by a wide margin in both simulation drag and novelty. Compared to the best baseline TripNet, 3DID reduces Sim Drag from 0.4066 to 0.3536, a 13.0% improvement, and lowers Pred Drag by 3.4% (from 0.2698 to 0.2607). It also increases novelty from 1.0683 to 1.1709, a 9.6% gain. In Figure 5, our continuous latent representation consistently yields watertight smooth geometries with superior aerodynamic performance, whereas voxel-based methods suffer higher drag and non-watertight artifacts. Although TripNet embeds continuous geometry, its optimized designs remain inferior. We attribute this to the absence of physical field guidance, which weakens the optimization gradients in the refinement stage.

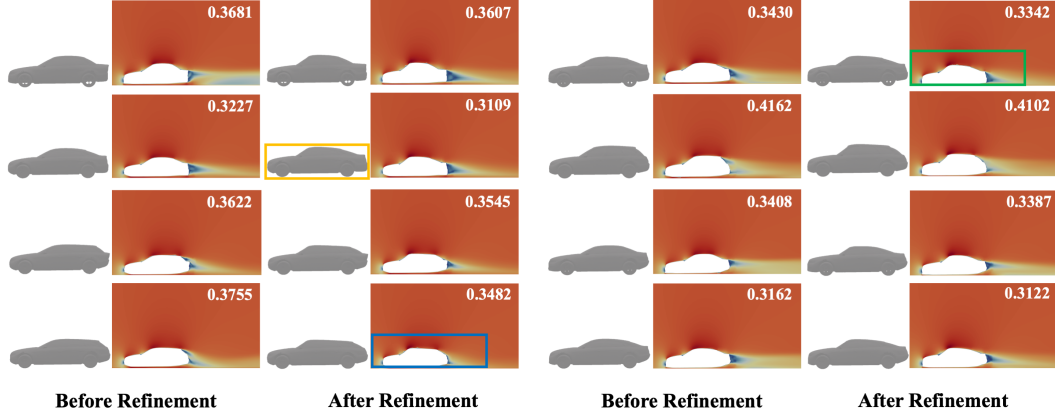


Figure 5: **Qualitative comparisons of topology-preserving refinement.** Each row presents two design candidates comparisons with their geometry and simulated velocity field heatmaps. Sim-Drag values are shown in the top-right corner of each panel. Refined designs exhibit a more significant fastback profile (yellow box), reduced low-velocity recirculation zones (blue box), and stronger downward flow (green box), indicating improved aerodynamic performance.

Table 3: **Ablation study on design strategies.**

Method	Pred-Drag↓	Sim-Drag↓	Novelty↑	Coverage↑
CEM	0.3152	0.3987	1.0730	0.6800
GD	0.3023	0.4095	1.0878	0.5800
W/O Guidance	0.2971	0.3944	0.9177	0.7104
3DID–NoTopoRefine (ours)	0.2623	0.3766	0.9195	0.6950
3DID (ours)	0.2607	0.3536	1.1709	0.4300

4.4 Ablation Study on Two-Stage Optimization Strategy

In this experiment, we validate the effectiveness of our two-stage optimization pipeline by comparing it against two alternative design strategies, including Cross-Entropy Method (CEM) and gradient descent (GD), as well as a diffusion-only sampling approach without objective gradient guidance. All methods are based on our physics-geometry unified representation.

From Table 3, we see that our full 3DID outperforms all baselines in Pred-Drag, Sim-Drag, and Novelty. Notably, when designing without guidance, our diffusion model attains the highest coverage value of 0.7104, as it captures the data manifold comprehensively. When generating without guidance, the diffusion model tends to mimic the distribution of the dataset, which leads to an increase of coverage but lacks the targeted optimization for aerodynamic performance and novelty that our 3DID method provides. Furthermore, to better validate the effectiveness of our topology-preserving refinement stage, we provide side-by-side qualitative comparisons in Figure 5. It can be seen that after the refinement stage, each candidate develops a more significant fastback profile, with diminished low-velocity recirculation regions, and stronger downward flow patterns, all indicators of improved aerodynamic performance as confirmed by the reduced Sim-Drag values.

5 Limitations

Limited to static physical fields. Despite the fact that 3DID achieves impressive results, a significant limitation is its focus on static fields. The current framework does not support inverse design involving time-dependent or dynamic physical fields. Time-dependent physical systems often involve solid geometries coupled with evolving physical properties over time. This would pose challenges for representation and optimization within our framework. Enhancing 3DID with time-aware representations and models may address these limitations, which we leave as an important direction for future work.

Limited to single objective optimization. In 3DID, we address the inverse problem with a single objective, which may limit its applicability for broader scenarios. Although it is straightforward to aggregate multiple objectives into a single composite loss, this approach may overlook potential conflicts and trade-offs between objectives. Extending 3DID to support true multi-objective optimization is a promising direction for future research.

Limited to surrogate-based physics awareness. We incorporate physical fields via data-driven surrogates and joint geometry–physics embeddings during generation and refinement, rather than enforcing governing laws explicitly. This guides designs toward plausible, high-performing regions but does not enforce hard physical constraints. Exploring hard-constraint mechanisms or tighter PDE-consistent couplings is an important direction for future work.

6 Conclusion

In this paper, we tackle the problem of 3D inverse design, which faces challenges from the high-dimensional physics–geometry coupling and the exploration–validity trade-off. To represent the coupled space, we propose a physics–geometry unified representation that preserves fine-grained shape details and physical-field information while significantly reducing dimensionality. Based on this representation, we introduce a two-stage physics-aware optimization strategy that first explores the latent manifold via gradient-guided diffusion sampling and then refines candidates through topology-preserving refinement. Extensive experiments demonstrate that our 3DID framework generates high-fidelity 3D models with greater versatility and superior performance on target objectives.

Acknowledgments

This work is partially supported by National Science and Technology Major Project (2022ZD0117802). This work was also supported in part by "Pioneer" and "Leading Goose" R&D Program of Zhejiang (No. 2025C02032), the Fundamental Research Funds for the Central Universities (226-2025-00080), and the Earth System Big Data Platform of the School of Earth Sciences, Zhejiang University.

References

- [1] Binyang Song, Chenyang Yuan, Frank Permenter, Nikos Arechiga, and Faez Ahmed. Surrogate modeling of car drag coefficient with depth and normal renderings. In *International Design Engineering Technical Conferences and Computers and Information in Engineering Conference*, volume 87301, page V03AT03A029. American Society of Mechanical Engineers, 2023.
- [2] Sean Molesky, Zin Lin, Alexander Y Piggott, Weiliang Jin, Jelena Vucković, and Alejandro W Rodriguez. Inverse design in nanophotonics. *Nature Photonics*, 12(11):659–670, 2018.
- [3] Jan-Hendrik Bastek and Dennis M Kochmann. Inverse design of nonlinear mechanical metamaterials via video denoising diffusion models. *Nature Machine Intelligence*, 5(12):1466–1475, 2023.
- [4] Claudio Zeni, Robert Pinsler, Daniel Zügner, Andrew Fowler, Matthew Horton, Xiang Fu, Zilong Wang, Aliaksandra Shysheya, Jonathan Crabbé, Shoko Ueda, et al. A generative model for inorganic materials design. *Nature*, pages 1–3, 2025.
- [5] Ann-Kathrin Schuetz, AWP Poon, and Aobo Li. Resum: A rare event surrogate model for physics detector design. In *International Conference on Learning Representations (ICLR)*.
- [6] W Kyle Anderson and V Venkatakrishnan. Aerodynamic design optimization on unstructured grids with a continuous adjoint formulation. *Computers & Fluids*, 28(4-5):443–480, 1999.
- [7] Chae M Rhie and Wei-Liang Chow. Numerical study of the turbulent flow past an airfoil with trailing edge separation. *AIAA journal*, 21(11):1525–1532, 1983.
- [8] Martin Philip Bendsoe and Ole Sigmund. *Topology optimization: theory, methods, and applications*. Springer Science & Business Media, 2013.

- [9] Antony Jameson. Aerodynamic design via control theory. *Journal of scientific computing*, 3:233–260, 1988.
- [10] Max D Gunzburger. *Perspectives in flow control and optimization*. SIAM, 2002.
- [11] Nicolas Rosset, Guillaume Cordonnier, Regis Duvigneau, and Adrien Bousseau. Interactive design of 2d car profiles with aerodynamic feedback. In *Computer Graphics Forum*, volume 42, pages 427–437. Wiley Online Library, 2023.
- [12] Liane Makatura. *Pareto gamuts: Exploring optimal designs across varying contexts*. PhD thesis, Massachusetts Institute of Technology, 2020.
- [13] Antony Jameson. Aerodynamic shape optimization using the adjoint method. *Lectures at the Von Karman Institute, Brussels*, 6, 2003.
- [14] Gaetan KW Kenway, Charles A Mader, Ping He, and Joaquim RRA Martins. Effective adjoint approaches for computational fluid dynamics. *Progress in Aerospace Sciences*, 110:100542, 2019.
- [15] Lana Osusky, Howard Buckley, Thomas Reist, and David W Zingg. Drag minimization based on the navier–stokes equations using a newton–krylov approach. *AIAA Journal*, 53(6):1555–1577, 2015.
- [16] Timothy MS Jim, Ghifari A Faza, Pramudita S Palar, and Koji Shimoyama. Bayesian optimization of a low-boom supersonic wing planform. *AIAA journal*, 59(11):4514–4529, 2021.
- [17] Grégoire Mariethoz, Philippe Renard, and Jef Caers. Bayesian inverse problem and optimization with iterative spatial resampling. *Water Resources Research*, 46(11), 2010.
- [18] Kelsey Allen, Tatiana Lopez-Guevara, Kimberly L Stachenfeld, Alvaro Sanchez Gonzalez, Peter Battaglia, Jessica B Hamrick, and Tobias Pfaff. Inverse design for fluid-structure interactions using graph network simulators. *Advances in Neural Information Processing Systems*, 35:13759–13774, 2022.
- [19] Tailin Wu, Willie Neiswanger, Hongtao Zheng, Stefano Ermon, and Jure Leskovec. Uncertainty quantification for forward and inverse problems of pdes via latent global evolution. In *Proceedings of the AAAI Conference on Artificial Intelligence*, volume 38, pages 320–328, 2024.
- [20] Tailin Wu, Takashi Maruyama, and Jure Leskovec. Learning to accelerate partial differential equations via latent global evolution. *Advances in Neural Information Processing Systems*, 35:2240–2253, 2022.
- [21] Qian Chen, Mohamed Elrefaie, Angela Dai, and Faez Ahmed. Tripnet: Learning large-scale high-fidelity 3d car aerodynamics with triplane networks. *arXiv preprint arXiv:2503.17400*, 2025.
- [22] Jonathan Tran, Kai Fukami, Kenta Inada, Daisuke Umehara, Yoshimichi Ono, Kenta Ogawa, and Kunihiro Taira. Aerodynamics-guided machine learning for design optimization of electric vehicles. *Communications Engineering*, 3(1):174, 2024.
- [23] Nikita Durasov, Artem Lukoyanov, Jonathan Donier, and Pascal Fua. Debosh: Deep bayesian shape optimization. *arXiv preprint arXiv:2109.13337*, 2021.
- [24] Pierre Baque, Edoardo Remelli, Francois Fleuret, and Pascal Fua. Geodesic convolutional shape optimization. In *International Conference on Machine Learning*, pages 472–481. PMLR, 2018.
- [25] Qingqing Zhao, David B Lindell, and Gordon Wetzstein. Learning to solve pde-constrained inverse problems with graph networks. *arXiv preprint arXiv:2206.00711*, 2022.
- [26] Tailin Wu, Takashi Maruyama, Long Wei, Tao Zhang, Yilun Du, Gianluca Iaccarino, and Jure Leskovec. Compositional generative inverse design. In *International Conference on Learning Representations (ICLR)*, 2024.

- [27] Jan Pawel Stanczuk, Georgios Batzolis, Teo Deveney, and Carola-Bibiane Schönlieb. Diffusion models encode the intrinsic dimension of data manifolds. In *International Conference on Machine Learning (ICML)*, 2024.
- [28] John David Anderson, John Wendt, et al. *Computational fluid dynamics*, volume 206. Springer, 1995.
- [29] Maziar Raissi, Paris Perdikaris, and George E Karniadakis. Physics-informed neural networks: A deep learning framework for solving forward and inverse problems involving nonlinear partial differential equations. *Journal of Computational physics*, 378:686–707, 2019.
- [30] Tobias Pfaff, Meire Fortunato, Alvaro Sanchez-Gonzalez, and Peter Battaglia. Learning mesh-based simulation with graph networks. In *International Conference on Learning Representations (ICLR)*, 2020.
- [31] Zongyi Li, Nikola Kovachki, Kamyar Azizzadenesheli, Burigede Liu, Kaushik Bhattacharya, Andrew Stuart, and Anima Anandkumar. Fourier neural operator for parametric partial differential equations. *arXiv preprint arXiv:2010.08895*, 2020.
- [32] Xihang Yue, Linchao Zhu, and Yi Yang. Deltaphi: Learning physical trajectory residual for pde solving. *arXiv preprint arXiv:2406.09795*, 2024.
- [33] Xihang Yue, Yi Yang, and Linchao Zhu. Holistic physics solver: Learning pdes in a unified spectral-physical space. In *Forty-second International Conference on Machine Learning*, 2025.
- [34] Navid Ansari, Hans-Peter Seidel, Nima Vahidi Ferdowsi, and Vahid Babaei. Autoinverse: Uncertainty aware inversion of neural networks. *Advances in Neural Information Processing Systems*, 35:8675–8686, 2022.
- [35] Changyu Deng, Yizhou Wang, Can Qin, Yun Fu, and Wei Lu. Self-directed online machine learning for topology optimization. *Nature communications*, 13(1):388, 2022.
- [36] Stelian Coros, Bernhard Thomaszewski, Gioacchino Noris, Shinjiro Sueda, Moira Forberg, Robert W Sumner, Wojciech Matusik, and Bernd Bickel. Computational design of mechanical characters. *ACM Transactions on Graphics (TOG)*, 32(4):1–12, 2013.
- [37] Zekun Ren, Siyu Isaac Parker Tian, Juhwan Noh, Felipe Oviedo, Guangzong Xing, Jiali Li, Qiaohao Liang, Ruiming Zhu, Armin G Aberle, Shijing Sun, et al. An invertible crystallographic representation for general inverse design of inorganic crystals with targeted properties. *Matter*, 5(1):314–335, 2022.
- [38] Claudio Zeni, Robert Pinsler, Daniel Zügner, Andrew Fowler, Matthew Horton, Xiang Fu, Sasha Shysheya, Jonathan Crabbé, Lixin Sun, Jake Smith, et al. Mattergen: a generative model for inorganic materials design. *arXiv preprint arXiv:2312.03687*, 2023.
- [39] Alex Zunger. Inverse design in search of materials with target functionalities. *Nature Reviews Chemistry*, 2(4):0121, 2018.
- [40] Arghya Bhowmik, Ivano E Castelli, Juan Maria Garcia-Lastra, Peter Bjørn Jørgensen, Ole Winther, and Tejs Vegge. A perspective on inverse design of battery interphases using multi-scale modelling, experiments and generative deep learning. *Energy Storage Materials*, 21:446–456, 2019.
- [41] Yifei Li, Yuchen Sun, Pingchuan Ma, Eftychios Sifakis, Tao Du, Bo Zhu, and Wojciech Matusik. Neuralfluid: Neural fluidic system design and control with differentiable simulation. In *Advances in Neural Information Processing Systems (NeurIPS)*.
- [42] Tiejun Li, Junjun Yan, Xinhai Chen, Zhichao Wang, Qingyang Zhang, Enqiang Zhou, Chunye Gong, and Jie Liu. Accelerating aerodynamic design optimization based on graph convolutional neural network. *International Journal of Modern Physics C*, 35(01):2450007, 2024.
- [43] Reuven Y Rubinstein and Dirk P Kroese. *The cross-entropy method: a unified approach to combinatorial optimization, Monte-Carlo simulation and machine learning*. Springer Science & Business Media, 2004.

- [44] Peter ZG Qian and CF Jeff Wu. Bayesian hierarchical modeling for integrating low-accuracy and high-accuracy experiments. *Technometrics*, 50(2):192–204, 2008.
- [45] Yuanming Hu, Luke Anderson, Tzu-Mao Li, Qi Sun, Nathan Carr, Jonathan Ragan-Kelley, and Frédo Durand. DiffTaichi: Differentiable programming for physical simulation. *arXiv preprint arXiv:1910.00935*, 2019.
- [46] Kazuo Yonekura, Kazunari Wada, and Katsuyuki Suzuki. Generating various airfoils with required lift coefficients by combining naca and joukowski airfoils using conditional variational autoencoders. *Engineering Applications of Artificial Intelligence*, 108:104560, 2022.
- [47] Wei Chen, Kevin Chiu, and Mark D Fuge. Airfoil design parameterization and optimization using bézier generative adversarial networks. *AIAA journal*, 58(11):4723–4735, 2020.
- [48] Gabriel Achour, Woong Je Sung, Olivia J Pinon-Fischer, and Dimitri N Mavris. Development of a conditional generative adversarial network for airfoil shape optimization. In *AIAA Scitech 2020 Forum*, page 2261, 2020.
- [49] Jian Liu, Jianyu Wu, Hairun Xie, Jing Wang, Liu Wei, Wanli Ouyang, Junjun Jiang, Xianming Liu, SHIXIANG TANG, Miao Zhang, et al. Afbench: A large-scale benchmark for airfoil design. *Advances in Neural Information Processing Systems (NeurIPS)*, 37:82757–82780, 2024.
- [50] Jichao Li, Xiaosong Du, and Joaquim RRA Martins. Machine learning in aerodynamic shape optimization. *Progress in Aerospace Sciences*, 134:100849, 2022.
- [51] Xinghui Yan, Jihong Zhu, Minchi Kuang, and Xiangyang Wang. Aerodynamic shape optimization using a novel optimizer based on machine learning techniques. *Aerospace Science and Technology*, 86:826–835, 2019.
- [52] Stephan Schmidt, Caslav Ilic, Volker Schulz, and Nicolas R Gauger. Three-dimensional large-scale aerodynamic shape optimization based on shape calculus. *AIAA journal*, 51(11):2615–2627, 2013.
- [53] Xiaolong He, Jichao Li, Charles A Mader, Anil Yildirim, and Joaquim RRA Martins. Robust aerodynamic shape optimization—from a circle to an airfoil. *Aerospace Science and Technology*, 87:48–61, 2019.
- [54] Nikos Arechiga, Frank Permenter, Binyang Song, and Chenyang Yuan. Drag-guided diffusion models for vehicle image generation. *arXiv preprint arXiv:2306.09935*, 2023.
- [55] Jichao Li and Jinsheng Cai. Massively multipoint aerodynamic shape design via surrogate-assisted gradient-based optimization. *AIAA Journal*, 58(5):1949–1963, 2020.
- [56] Jichao Li and Mengqi Zhang. Adjoint-free aerodynamic shape optimization of the common research model wing. *AIAA Journal*, 59(6):1990–2000, 2021.
- [57] Thomas P Dussauge, Woong Je Sung, Olivia J Pinon Fischer, and Dimitri N Mavris. A reinforcement learning approach to airfoil shape optimization. *Scientific Reports*, 13(1):9753, 2023.
- [58] Mohamed Amine Bouhlel, Sicheng He, and Joaquim RRA Martins. Scalable gradient-enhanced artificial neural networks for airfoil shape design in the subsonic and transonic regimes. *Structural and Multidisciplinary Optimization*, 61(4):1363–1376, 2020.
- [59] Xiaosong Du, Ping He, and Joaquim RRA Martins. A b-spline-based generative adversarial network model for fast interactive airfoil aerodynamic optimization. In *AIAA scitech 2020 forum*, page 2128, 2020.
- [60] Shuang Wu, Youtian Lin, Feihu Zhang, Yifei Zeng, Jingxi Xu, Philip Torr, Xun Cao, and Yao Yao. Direct3d: Scalable image-to-3d generation via 3d latent diffusion transformer. *Advances in Neural Information Processing Systems (NeurIPS)*, 2024.
- [61] Andrew Jaegle, Felix Gimeno, Andy Brock, Oriol Vinyals, Andrew Zisserman, and Joao Carreira. Perceiver: General perception with iterative attention. In *International Conference on Machine Learning (ICML)*, pages 4651–4664. PMLR, 2021.

- [62] Tengfei Wang, Bo Zhang, Ting Zhang, Shuyang Gu, Jianmin Bao, Tadas Baltrusaitis, Jingjing Shen, Dong Chen, Fang Wen, Qifeng Chen, et al. Rodin: A generative model for sculpting 3d digital avatars using diffusion. In *Proceedings of the Conference on Computer Vision and Pattern Recognition (CVPR)*, pages 4563–4573, 2023.
- [63] Jonathan Ho, Ajay Jain, and Pieter Abbeel. Denoising diffusion probabilistic models. *Advances in neural information processing systems*, 33:6840–6851, 2020.
- [64] Jiaming Song, Chenlin Meng, and Stefano Ermon. Denoising diffusion implicit models. *arXiv preprint arXiv:2010.02502*, 2020.
- [65] Hyungjin Chung, Jeongsol Kim, Michael T Mccann, Marc L Klasky, and Jong Chul Ye. Diffusion posterior sampling for general noisy inverse problems. *arXiv preprint arXiv:2209.14687*, 2022.
- [66] Arpit Bansal, Hong-Min Chu, Avi Schwarzschild, Soumyadip Sengupta, Micah Goldblum, Jonas Geiping, and Tom Goldstein. Universal guidance for diffusion models. In *Proceedings of the Conference on Computer Vision and Pattern Recognition (CVPR)*, pages 843–852, 2023.
- [67] Gentaro Hirota, Renee Maheshwari, and Ming C Lin. Fast volume-preserving free form deformation using multi-level optimization. In *Proceedings of the fifth ACM symposium on Solid modeling and applications*, pages 234–245, 1999.
- [68] William M Hsu, John F Hughes, and Henry Kaufman. Direct manipulation of free-form deformations. *ACM Siggraph Computer Graphics*, 26(2):177–184, 1992.
- [69] Kaiming He, Xiangyu Zhang, Shaoqing Ren, and Jian Sun. Deep residual learning for image recognition. In *Proceedings of the Conference on Computer Vision and Pattern Recognition (CVPR)*, pages 770–778, 2016.
- [70] William Peebles and Saining Xie. Scalable diffusion models with transformers. In *Proceedings of the International Conference on Computer Vision (ICCV)*, pages 4195–4205, 2023.
- [71] Ilya Loshchilov and Frank Hutter. Decoupled weight decay regularization. *arXiv preprint arXiv:1711.05101*, 2017.
- [72] Mohamed Elrefaie, Florin Morar, Angela Dai, and Faez Ahmed. Drivaernet++: A large-scale multimodal car dataset with computational fluid dynamics simulations and deep learning benchmarks. *Advances in Neural Information Processing Systems (NeurIPS)*, 37:499–536, 2024.
- [73] Mohamed Elrefaie, Angela Dai, and Faez Ahmed. Drivaernet: A parametric car dataset for data-driven aerodynamic design and graph-based drag prediction. In *International Design Engineering Technical Conferences and Computers and Information in Engineering Conference*, volume 88360, page V03AT03A019. American Society of Mechanical Engineers, 2024.
- [74] Jeong Joon Park, Peter Florence, Julian Straub, Richard Newcombe, and Steven Lovegrove. DeepSDF: Learning continuous signed distance functions for shape representation. In *Proceedings of the Conference on Computer Vision and Pattern Recognition (CVPR)*, pages 165–174, 2019.
- [75] Alex Nichol, Heewoo Jun, Pratul Dhariwal, Pamela Mishkin, and Mark Chen. Point-e: A system for generating 3d point clouds from complex prompts. *arXiv preprint arXiv:2212.08751*, 2022.
- [76] Premith Kumar Chilukuri, Binyang Song, SungKu Kang, and Ran Jin. Generating optimized 3d designs for manufacturing using a guided voxel diffusion model. In *International Manufacturing Science and Engineering Conference*, volume 88117, page V002T07A006. American Society of Mechanical Engineers, 2024.
- [77] Diederik P Kingma, Max Welling, et al. Auto-encoding variational bayes, 2013.
- [78] Hervé Abdi and Lynne J Williams. Principal component analysis. *Wiley interdisciplinary reviews: computational statistics*, 2(4):433–459, 2010.

- [79] Christopher Greenshields. *OpenFOAM v11 User Guide*. The OpenFOAM Foundation, London, UK, 2023.
- [80] Florian R Menter, Martin Kuntz, Robin Langtry, et al. Ten years of industrial experience with the sst turbulence model. *Turbulence, heat and mass transfer*, 4(1):625–632, 2003.

NeurIPS Paper Checklist

1. Claims

Question: Do the main claims made in the abstract and introduction accurately reflect the paper's contributions and scope?

Answer: [\[Yes\]](#)

Justification: In this paper, we propose a novel 3D inverse-design framework that can directly navigate the full 3D design space. Extensive experiments in aerodynamic shape optimization demonstrate the effectiveness of our 3DID framework.

Guidelines:

- The answer NA means that the abstract and introduction do not include the claims made in the paper.
- The abstract and/or introduction should clearly state the claims made, including the contributions made in the paper and important assumptions and limitations. A No or NA answer to this question will not be perceived well by the reviewers.
- The claims made should match theoretical and experimental results, and reflect how much the results can be expected to generalize to other settings.
- It is fine to include aspirational goals as motivation as long as it is clear that these goals are not attained by the paper.

2. Limitations

Question: Does the paper discuss the limitations of the work performed by the authors?

Answer: [\[Yes\]](#)

Justification: The limitations of 3DID are detailed in the main paper (Sec. 5).

Guidelines:

- The answer NA means that the paper has no limitation while the answer No means that the paper has limitations, but those are not discussed in the paper.
- The authors are encouraged to create a separate "Limitations" section in their paper.
- The paper should point out any strong assumptions and how robust the results are to violations of these assumptions (e.g., independence assumptions, noiseless settings, model well-specification, asymptotic approximations only holding locally). The authors should reflect on how these assumptions might be violated in practice and what the implications would be.
- The authors should reflect on the scope of the claims made, e.g., if the approach was only tested on a few datasets or with a few runs. In general, empirical results often depend on implicit assumptions, which should be articulated.
- The authors should reflect on the factors that influence the performance of the approach. For example, a facial recognition algorithm may perform poorly when image resolution is low or images are taken in low lighting. Or a speech-to-text system might not be used reliably to provide closed captions for online lectures because it fails to handle technical jargon.
- The authors should discuss the computational efficiency of the proposed algorithms and how they scale with dataset size.
- If applicable, the authors should discuss possible limitations of their approach to address problems of privacy and fairness.
- While the authors might fear that complete honesty about limitations might be used by reviewers as grounds for rejection, a worse outcome might be that reviewers discover limitations that aren't acknowledged in the paper. The authors should use their best judgment and recognize that individual actions in favor of transparency play an important role in developing norms that preserve the integrity of the community. Reviewers will be specifically instructed to not penalize honesty concerning limitations.

3. Theory assumptions and proofs

Question: For each theoretical result, does the paper provide the full set of assumptions and a complete (and correct) proof?

Answer: [NA]

Justification: The paper does not include theoretical results.

Guidelines:

- The answer NA means that the paper does not include theoretical results.
- All the theorems, formulas, and proofs in the paper should be numbered and cross-referenced.
- All assumptions should be clearly stated or referenced in the statement of any theorems.
- The proofs can either appear in the main paper or the supplemental material, but if they appear in the supplemental material, the authors are encouraged to provide a short proof sketch to provide intuition.
- Inversely, any informal proof provided in the core of the paper should be complemented by formal proofs provided in appendix or supplemental material.
- Theorems and Lemmas that the proof relies upon should be properly referenced.

4. Experimental result reproducibility

Question: Does the paper fully disclose all the information needed to reproduce the main experimental results of the paper to the extent that it affects the main claims and/or conclusions of the paper (regardless of whether the code and data are provided or not)?

Answer: [Yes]

Justification: We provide a full description of 3DID's training setup and our dataset preparation pipeline in the Appendix.

Guidelines:

- The answer NA means that the paper does not include experiments.
- If the paper includes experiments, a No answer to this question will not be perceived well by the reviewers: Making the paper reproducible is important, regardless of whether the code and data are provided or not.
- If the contribution is a dataset and/or model, the authors should describe the steps taken to make their results reproducible or verifiable.
- Depending on the contribution, reproducibility can be accomplished in various ways. For example, if the contribution is a novel architecture, describing the architecture fully might suffice, or if the contribution is a specific model and empirical evaluation, it may be necessary to either make it possible for others to replicate the model with the same dataset, or provide access to the model. In general, releasing code and data is often one good way to accomplish this, but reproducibility can also be provided via detailed instructions for how to replicate the results, access to a hosted model (e.g., in the case of a large language model), releasing of a model checkpoint, or other means that are appropriate to the research performed.
- While NeurIPS does not require releasing code, the conference does require all submissions to provide some reasonable avenue for reproducibility, which may depend on the nature of the contribution. For example
 - (a) If the contribution is primarily a new algorithm, the paper should make it clear how to reproduce that algorithm.
 - (b) If the contribution is primarily a new model architecture, the paper should describe the architecture clearly and fully.
 - (c) If the contribution is a new model (e.g., a large language model), then there should either be a way to access this model for reproducing the results or a way to reproduce the model (e.g., with an open-source dataset or instructions for how to construct the dataset).
 - (d) We recognize that reproducibility may be tricky in some cases, in which case authors are welcome to describe the particular way they provide for reproducibility. In the case of closed-source models, it may be that access to the model is limited in some way (e.g., to registered users), but it should be possible for other researchers to have some path to reproducing or verifying the results.

5. Open access to data and code

Question: Does the paper provide open access to the data and code, with sufficient instructions to faithfully reproduce the main experimental results, as described in supplemental material?

Answer: [Yes]

Justification: Our code will be open-sourced and available on GitHub upon publication.

Guidelines:

- The answer NA means that paper does not include experiments requiring code.
- Please see the NeurIPS code and data submission guidelines (<https://nips.cc/public/guides/CodeSubmissionPolicy>) for more details.
- While we encourage the release of code and data, we understand that this might not be possible, so “No” is an acceptable answer. Papers cannot be rejected simply for not including code, unless this is central to the contribution (e.g., for a new open-source benchmark).
- The instructions should contain the exact command and environment needed to run to reproduce the results. See the NeurIPS code and data submission guidelines (<https://nips.cc/public/guides/CodeSubmissionPolicy>) for more details.
- The authors should provide instructions on data access and preparation, including how to access the raw data, preprocessed data, intermediate data, and generated data, etc.
- The authors should provide scripts to reproduce all experimental results for the new proposed method and baselines. If only a subset of experiments are reproducible, they should state which ones are omitted from the script and why.
- At submission time, to preserve anonymity, the authors should release anonymized versions (if applicable).
- Providing as much information as possible in supplemental material (appended to the paper) is recommended, but including URLs to data and code is permitted.

6. Experimental setting/details

Question: Does the paper specify all the training and test details (e.g., data splits, hyperparameters, how they were chosen, type of optimizer, etc.) necessary to understand the results?

Answer: [Yes]

Justification: The details of training and evaluation are included in Appendix.

Guidelines:

- The answer NA means that the paper does not include experiments.
- The experimental setting should be presented in the core of the paper to a level of detail that is necessary to appreciate the results and make sense of them.
- The full details can be provided either with the code, in appendix, or as supplemental material.

7. Experiment statistical significance

Question: Does the paper report error bars suitably and correctly defined or other appropriate information about the statistical significance of the experiments?

Answer: [Yes]

Justification: The confidence interval information is detailed in the Appendix.

Guidelines:

- The answer NA means that the paper does not include experiments.
- The authors should answer "Yes" if the results are accompanied by error bars, confidence intervals, or statistical significance tests, at least for the experiments that support the main claims of the paper.
- The factors of variability that the error bars are capturing should be clearly stated (for example, train/test split, initialization, random drawing of some parameter, or overall run with given experimental conditions).
- The method for calculating the error bars should be explained (closed form formula, call to a library function, bootstrap, etc.)

- The assumptions made should be given (e.g., Normally distributed errors).
- It should be clear whether the error bar is the standard deviation or the standard error of the mean.
- It is OK to report 1-sigma error bars, but one should state it. The authors should preferably report a 2-sigma error bar than state that they have a 96% CI, if the hypothesis of Normality of errors is not verified.
- For asymmetric distributions, the authors should be careful not to show in tables or figures symmetric error bars that would yield results that are out of range (e.g. negative error rates).
- If error bars are reported in tables or plots, The authors should explain in the text how they were calculated and reference the corresponding figures or tables in the text.

8. Experiments compute resources

Question: For each experiment, does the paper provide sufficient information on the computer resources (type of compute workers, memory, time of execution) needed to reproduce the experiments?

Answer: [Yes]

Justification: The details of compute resources are included in Appendix.

Guidelines:

- The answer NA means that the paper does not include experiments.
- The paper should indicate the type of compute workers CPU or GPU, internal cluster, or cloud provider, including relevant memory and storage.
- The paper should provide the amount of compute required for each of the individual experimental runs as well as estimate the total compute.
- The paper should disclose whether the full research project required more compute than the experiments reported in the paper (e.g., preliminary or failed experiments that didn't make it into the paper).

9. Code of ethics

Question: Does the research conducted in the paper conform, in every respect, with the NeurIPS Code of Ethics <https://neurips.cc/public/EthicsGuidelines>?

Answer: [Yes]

Justification: We have reviewed the Code of Ethics and it conforms with the Code of Ethics.

Guidelines:

- The answer NA means that the authors have not reviewed the NeurIPS Code of Ethics.
- If the authors answer No, they should explain the special circumstances that require a deviation from the Code of Ethics.
- The authors should make sure to preserve anonymity (e.g., if there is a special consideration due to laws or regulations in their jurisdiction).

10. Broader impacts

Question: Does the paper discuss both potential positive societal impacts and negative societal impacts of the work performed?

Answer: [Yes]

Justification: The details of broader impacts are included in Appendix.

Guidelines:

- The answer NA means that there is no societal impact of the work performed.
- If the authors answer NA or No, they should explain why their work has no societal impact or why the paper does not address societal impact.
- Examples of negative societal impacts include potential malicious or unintended uses (e.g., disinformation, generating fake profiles, surveillance), fairness considerations (e.g., deployment of technologies that could make decisions that unfairly impact specific groups), privacy considerations, and security considerations.

- The conference expects that many papers will be foundational research and not tied to particular applications, let alone deployments. However, if there is a direct path to any negative applications, the authors should point it out. For example, it is legitimate to point out that an improvement in the quality of generative models could be used to generate deepfakes for disinformation. On the other hand, it is not needed to point out that a generic algorithm for optimizing neural networks could enable people to train models that generate Deepfakes faster.
- The authors should consider possible harms that could arise when the technology is being used as intended and functioning correctly, harms that could arise when the technology is being used as intended but gives incorrect results, and harms following from (intentional or unintentional) misuse of the technology.
- If there are negative societal impacts, the authors could also discuss possible mitigation strategies (e.g., gated release of models, providing defenses in addition to attacks, mechanisms for monitoring misuse, mechanisms to monitor how a system learns from feedback over time, improving the efficiency and accessibility of ML).

11. Safeguards

Question: Does the paper describe safeguards that have been put in place for responsible release of data or models that have a high risk for misuse (e.g., pretrained language models, image generators, or scraped datasets)?

Answer: [NA]

Justification: Our model focus on 3D inverse design, with minimal risk of misuse.

Guidelines:

- The answer NA means that the paper poses no such risks.
- Released models that have a high risk for misuse or dual-use should be released with necessary safeguards to allow for controlled use of the model, for example by requiring that users adhere to usage guidelines or restrictions to access the model or implementing safety filters.
- Datasets that have been scraped from the Internet could pose safety risks. The authors should describe how they avoided releasing unsafe images.
- We recognize that providing effective safeguards is challenging, and many papers do not require this, but we encourage authors to take this into account and make a best faith effort.

12. Licenses for existing assets

Question: Are the creators or original owners of assets (e.g., code, data, models), used in the paper, properly credited and are the license and terms of use explicitly mentioned and properly respected?

Answer: [Yes]

Justification: The licenses are mentioned in Appendix.

Guidelines:

- The answer NA means that the paper does not use existing assets.
- The authors should cite the original paper that produced the code package or dataset.
- The authors should state which version of the asset is used and, if possible, include a URL.
- The name of the license (e.g., CC-BY 4.0) should be included for each asset.
- For scraped data from a particular source (e.g., website), the copyright and terms of service of that source should be provided.
- If assets are released, the license, copyright information, and terms of use in the package should be provided. For popular datasets, paperswithcode.com/datasets has curated licenses for some datasets. Their licensing guide can help determine the license of a dataset.
- For existing datasets that are re-packaged, both the original license and the license of the derived asset (if it has changed) should be provided.

- If this information is not available online, the authors are encouraged to reach out to the asset’s creators.

13. **New assets**

Question: Are new assets introduced in the paper well documented and is the documentation provided alongside the assets?

Answer: [\[Yes\]](#)

Justification: The details of the model are provided in this paper.

Guidelines:

- The answer NA means that the paper does not release new assets.
- Researchers should communicate the details of the dataset/code/model as part of their submissions via structured templates. This includes details about training, license, limitations, etc.
- The paper should discuss whether and how consent was obtained from people whose asset is used.
- At submission time, remember to anonymize your assets (if applicable). You can either create an anonymized URL or include an anonymized zip file.

14. **Crowdsourcing and research with human subjects**

Question: For crowdsourcing experiments and research with human subjects, does the paper include the full text of instructions given to participants and screenshots, if applicable, as well as details about compensation (if any)?

Answer: [\[NA\]](#)

Justification: The paper does not involve crowdsourcing nor research with human subjects.

Guidelines:

- The answer NA means that the paper does not involve crowdsourcing nor research with human subjects.
- Including this information in the supplemental material is fine, but if the main contribution of the paper involves human subjects, then as much detail as possible should be included in the main paper.
- According to the NeurIPS Code of Ethics, workers involved in data collection, curation, or other labor should be paid at least the minimum wage in the country of the data collector.

15. **Institutional review board (IRB) approvals or equivalent for research with human subjects**

Question: Does the paper describe potential risks incurred by study participants, whether such risks were disclosed to the subjects, and whether Institutional Review Board (IRB) approvals (or an equivalent approval/review based on the requirements of your country or institution) were obtained?

Answer: [\[NA\]](#)

Justification: The paper does not involve crowdsourcing nor research with human subjects.

Guidelines:

- The answer NA means that the paper does not involve crowdsourcing nor research with human subjects.
- Depending on the country in which research is conducted, IRB approval (or equivalent) may be required for any human subjects research. If you obtained IRB approval, you should clearly state this in the paper.
- We recognize that the procedures for this may vary significantly between institutions and locations, and we expect authors to adhere to the NeurIPS Code of Ethics and the guidelines for their institution.
- For initial submissions, do not include any information that would break anonymity (if applicable), such as the institution conducting the review.

16. **Declaration of LLM usage**

Question: Does the paper describe the usage of LLMs if it is an important, original, or non-standard component of the core methods in this research? Note that if the LLM is used only for writing, editing, or formatting purposes and does not impact the core methodology, scientific rigorousness, or originality of the research, declaration is not required.

Answer: [NA]

Justification: LLM is only used for editing.

Guidelines:

- The answer NA means that the core method development in this research does not involve LLMs as any important, original, or non-standard components.
- Please refer to our LLM policy (<https://neurips.cc/Conferences/2025/LLM>) for what should or should not be described.

Appendix

In Appendix A, we provide additional experiments results.

- In Appendix A.1, we further provide the full results for 3D vehicle aerodynamic design.
- In Appendix A.2, we provide more visualization of design results.
- In Appendix A.3, we provide more qualitative comparisons of topology-preserving refinement.

Appendix B: The implementation details of baseline methods.

Appendix C: The dataset processing details.

Appendix D: The implementation details of 3DID.

Appendix E: The evaluation details of 3DID.

Appendix F: The broader impact of 3DID.

Appendix G: The licenses of datasets, codes, and models used in this paper.

A Additional Results

A.1 Full Results for 3D Vehicle Aerodynamic Design

Here we present the full statistical results of our experiments, including 95% confidence intervals for all compared methods, shown in Table 4. A box plot of the simulation-derived drag coefficient (Sim-Drag) is shown in Figure 6, illustrating the distribution, variability, and outlier behavior across different approaches.

Table 4: Quantitative comparison for aerodynamic vehicle design.

Method	Pred-Drag↓	Sim-Drag↓	Novelty↑	Coverage↑
GP, Voxel	0.2997±0.0436	0.4254 ± 0.0351	1.0399±0.0572	0.5200±0.0675
GP, Voxel+PCA	0.3059±0.0490	0.4363 ± 0.0425	0.9734±0.0195	0.5850±0.0675
CEM, Voxel	0.2951±0.0421	0.4097 ± 0.0279	0.9792±0.0213	0.4350±0.0676
CEM, Voxel+PCA	0.3088±0.0478	0.4393 ± 0.0469	0.9864±0.0250	0.5100±0.0600
CEM, TripNet	0.3154±0.0476	0.4161 ± 0.0415	1.0399±0.0323	0.6050± 0.0725
Backprop, Voxel	0.2979±0.0314	0.4146 ± 0.0244	0.9860±0.0204	0.4750±0.0675
Backprop, Voxel+PCA	0.3061±0.0576	0.4614 ± 0.0316	0.9798±0.0208	0.4950±0.0675
Backprop, TripNet	0.3153±0.0472	0.4170 ± 0.0444	1.0294±0.0290	0.5900±0.0700
3DID–NoTopoRefine (ours)	0.2623±0.0373	0.3766 ± 0.0393	0.9195±0.0213	0.6950 ±0.0627
3DID (ours)	0.2607 ±0.0331	0.3536 ± 0.0313	1.1709 ±0.0282	0.4300±0.0650

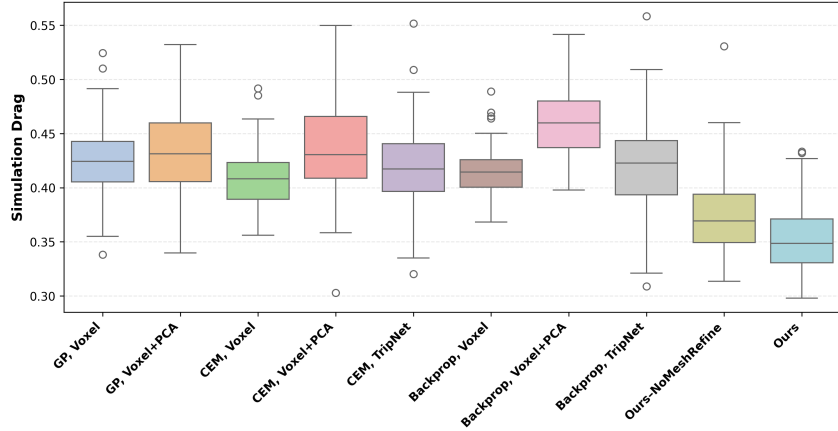


Figure 6: The box plot of the simulation-derived drag coefficient.

A.2 Visualization of 3DID Design

Additional visualizations of our designs are provided in Figure 7, where each design is shown alongside its geometry and corresponding physical fields.

A.3 Comparisons of Topology-Preserving Refinement

We provide additional qualitative comparisons in Figure 8 to demonstrate the effectiveness of our refinement stage. As shown, the design candidates consistently evolve toward a fastback profile after refinement, exhibiting reduced low-velocity recirculation regions and enhanced downward flow patterns, which indicate improved aerodynamic performance.

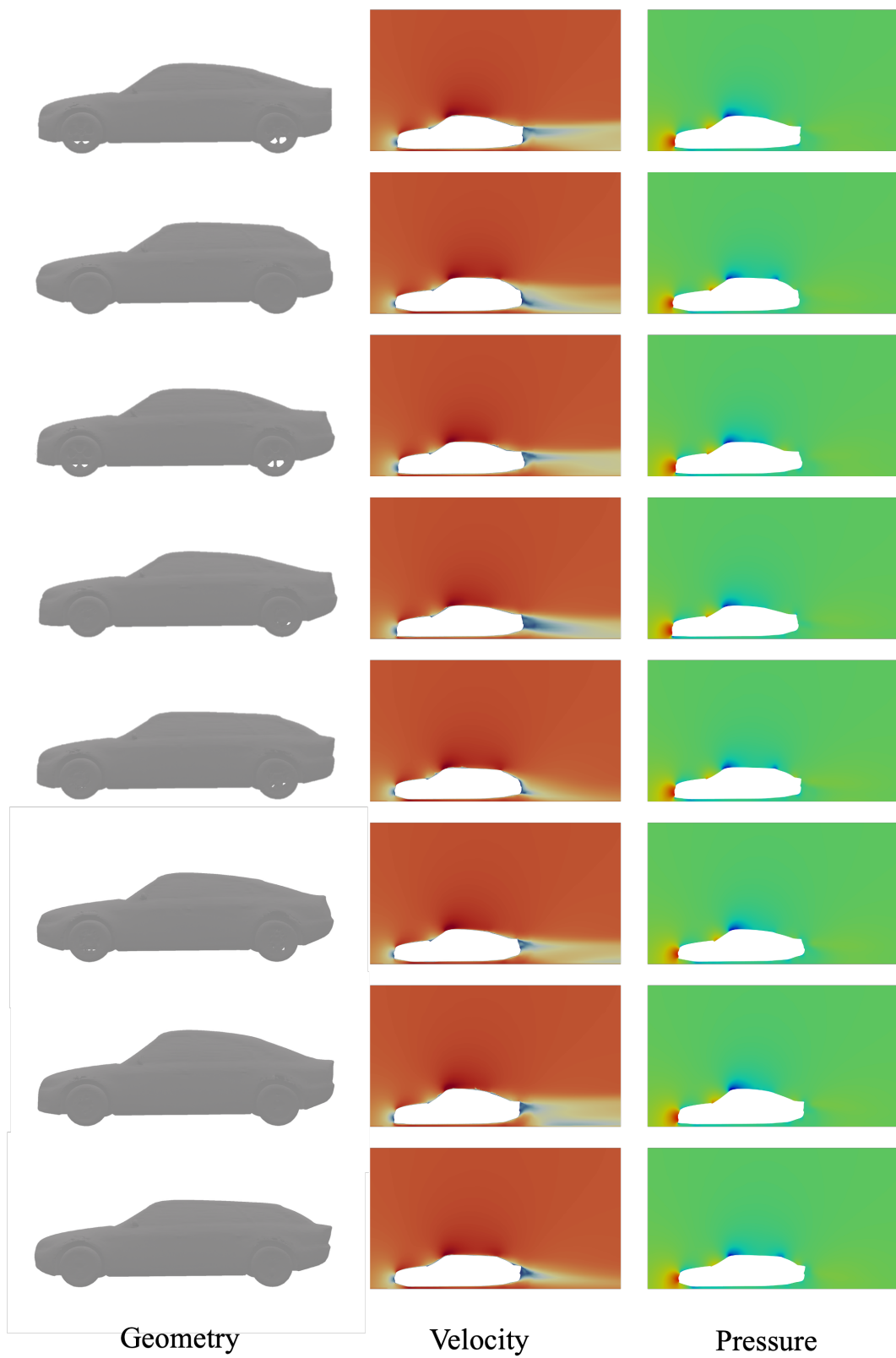


Figure 7: **Qualitative results of our 3DID.** Each row displays a design candidate along with its corresponding velocity and pressure field heatmaps.

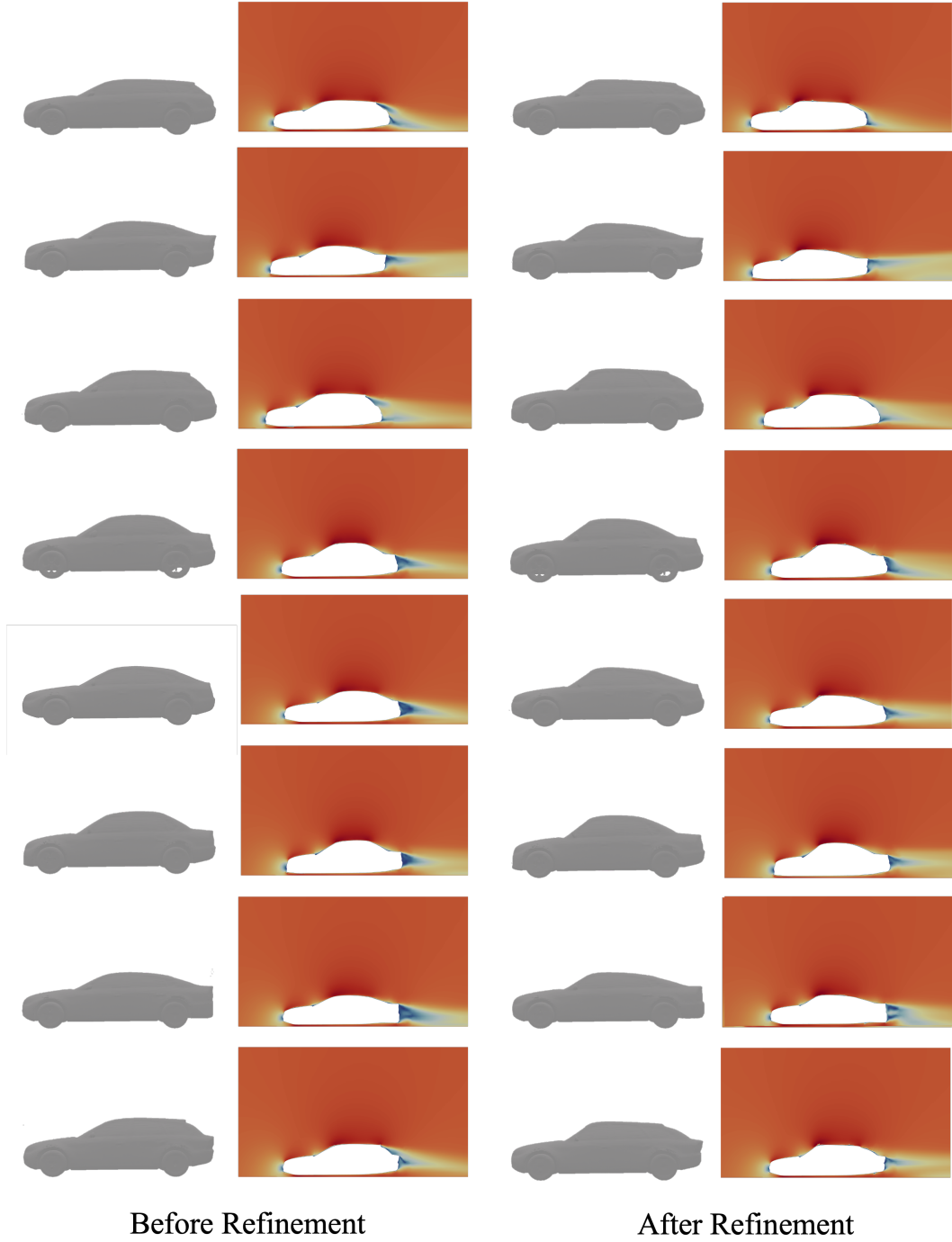


Figure 8: **Qualitative comparisons of topology-preserving refinement.** Each row presents two design candidates comparisons with their geometry and simulated velocity field heatmaps.

B Baseline implementation details

In our experiments, we compare our method against traditional sampling-based and backpropagation-based approaches using various design representations. As baselines, we include the Cross-Entropy Method (CEM) [43], the Gaussian-process surrogate with Bayesian optimization (GP) [44], and the gradient-based backpropagation method (Backprop) [18]. For representations, the optimizer is instantiated with three representations: a dense voxel grid [76], a PCA-compressed voxel grid (Voxel+PCA) [22], and a pure geometry triplane network (TripNet) [21]. For each representation, we train a VAE model [77] to compress the high-dimensional geometry into a compact latent code, which serves as the optimization space for inverse design.

B.1 Representation Baseline

Voxel. We train a voxel VAE [77] model directly on dense voxelized geometry to learn a latent embedding, as demonstrated in Figure 9. To train the model, we utilize the entire DrivAerNet++ [72] dataset, and voxelize the provided geometry with 256^3 resolution. For the Encoder, we leverage a sequence of 3D convolution layers followed by batch normalization and LeakyReLU to encode the voxel grid into a compact latent z_{voxel} . For voxel decoder, the latent vector z_{voxel} is first projected to a high-dimensional feature space and reshaped into a 3D tensor. A sequence of 3D transposed convolutional layers is then applied to reconstruct the voxel grid from this intermediate representation. Additionally, a separate drag prediction head, implemented as a multi-layer perceptron (MLP), is applied to estimate the target drag coefficient. We train the VAE model with reconstruction loss $\mathcal{L}_{\text{recon}}$, KL loss \mathcal{L}_{KL} , and the drag coefficient prediction loss $\mathcal{L}_{\text{drag}}$. The hyperparameters of the model and training are provided in Table 5

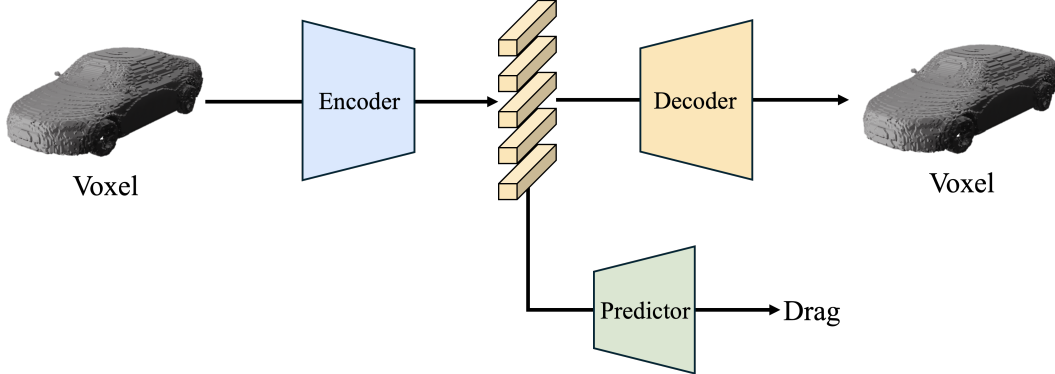


Figure 9: The overview of Voxel-VAE.

Voxel-PCA. Our Voxel-PCA representation is based on the representation proposed by [22] with modifications. In contrast to the Voxel-VAE, which directly uses voxel grids as input, the Voxel-PCA model first applies a dimensionality reduction step before downstream processing, as shown in Figure 10. Specifically, given the voxel data, we perform PCA [78] to obtain a compact representation of each geometry. Then, with this representation, we leverage a series of MLPs to encode the reduced features into a latent code $z_{\text{voxel-pca}}$. For reconstruction, an MLP decoder is first applied to reconstruct the PCA features from the latent code, which are then projected back to the voxel grid using the inverse PCA transformation. For drag prediction, similar to Voxel-VAE, a separate drag prediction head is applied to estimate the target drag coefficient. Our Voxel-PCA model is also trained with reconstruction loss $\mathcal{L}_{\text{recon}}$, KL loss \mathcal{L}_{KL} and drag prediction loss $\mathcal{L}_{\text{drag}}$. The hyperparameters of the model and training are provided in Table 6.

TripNet. Our TripNet representation is a pure geometry-based triplane representation, similar to the one proposed in [21], where it was used for forward prediction. The training procedure mirrors that of our unified physics-geometry framework, but excludes the physical field prediction branch, as illustrated in Figure 11. To obtain the representation, we utilize transformers with learnable tokens to extract features from the input point cloud. These features are then decoded using a transformer-based decoder and a geometry mapping network to predict the occupancy field of the design geometry. We

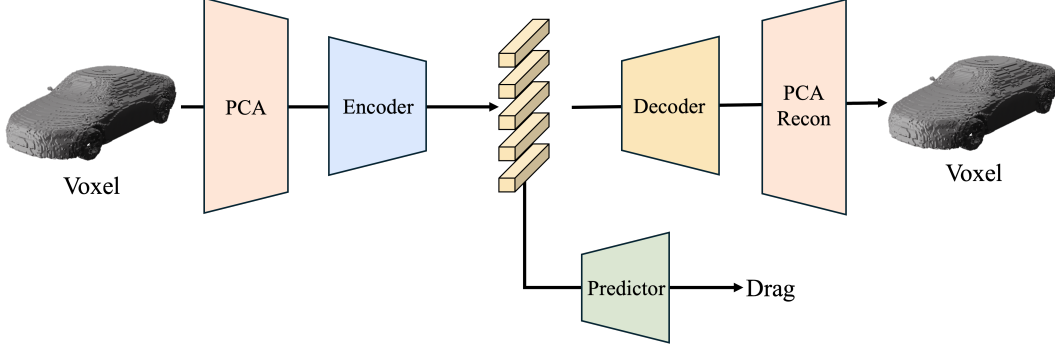


Figure 10: **The overview of Voxel-PCA-VAE.**

utilize the Binary Cross-Entropy loss \mathcal{L}_{BCE} and KL loss \mathcal{L}_{KL} to supervise the training of VAE. To further predict the drag coefficient, we adopt the same U-Net architecture used in our objective-guided diffusion model. The TripNet-VAE architecture adopts the same hyperparameter configuration as the geometry branch of our PG-VAE. More training hyperparameters are provided in Table 7.

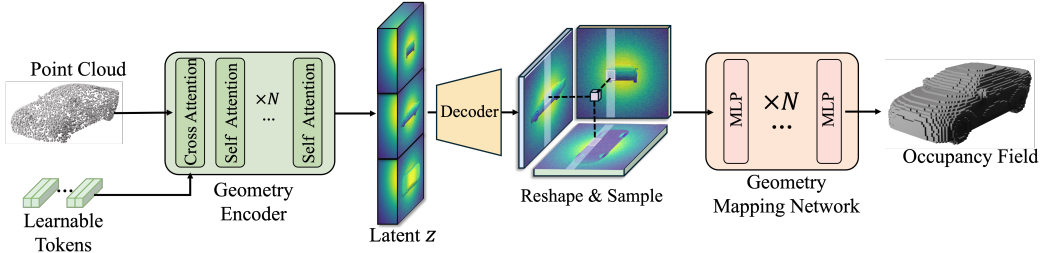


Figure 11: **The overview of TripNet-VAE.**

B.2 Optimization Baseline

CEM. Cross Entropy Method [43] is a traditional sampling-based optimization method widely used in classical inverse design problems. It starts with an initial distribution, and in each iteration, it samples multiple candidates from the current distribution. Then, these candidates are evaluated against the target objective function to select a subset of elite samples with the best performance. The distribution parameters are updated based on these elite samples. A smoothing coefficient controls the rate of distribution updates between iterations. This process continues until convergence or a maximum number of iterations is reached. In our experiment, we utilize a Gaussian distribution derived from encoded randomly selected samples as the initial distribution to provide a valid starting point.

GP. Gaussian-process surrogate with Bayesian optimization is a classical optimization method for black-box optimization [16, 17]. Bayesian optimization (BO) operates by constructing a probabilistic surrogate model, commonly a Gaussian-process model, to approximate the objective function based on past observations. At each iteration, an acquisition function is used to balance exploration of uncertain regions and exploitation of promising areas, guiding the selection of the next evaluation point. This strategy enables efficient optimization in high-cost or sample-limited scenarios by focusing evaluations on the most informative regions of the design space. While this method is effective in low-dimensional settings, constructing an accurate GP model becomes computationally expensive and challenging as the dimensionality of the design space increases. Therefore, GP-based Bayesian optimization is typically limited to small-scale or low-dimensional problems, where the surrogate can be reliably trained. In our experiment, our Gaussian process employs a Matérn kernel with constant and white noise components to model the objective function. At each iteration, Expected Improvement (EI) is used as the acquisition function.

Backprop. With the trained surrogate models, end-to-end backpropagation enables efficient gradient-based optimization of the design, leveraging the differentiability of the surrogate to guide updates [18, 19]. In our experiments, we use the trained drag predictor as the surrogate and update the latent code using the Adam optimizer.

C Dataset processing details.

In this work, we conduct experiments on DrivAerNet++ [72], which is the largest aerodynamic car design dataset, comprising diverse car designs with corresponding CFD simulations. To train our model, we use the dataset with 8085 car designs to extract the point cloud and physical field. We first normalize each geometry of cars to fit within a unit cube, then uniformly sample 50,000 points with corresponding normals from the geometry surface. For the physical field, we apply the same scaling factor to ensure alignment with the normalized geometry. Subsequently, we randomly sample 50,000 points within the unit cube and interpolate the physical field values at each location. These points serve as the input of our PG-VAE. For supervision, we additionally sample another 50,000 points, each annotated with both occupancy values and physical field data. In this work, we focus on the pressure and velocity fields for the physical field representation, as wall shear stress is defined only on the surface of the geometry and is thus not suitable for volumetric sampling. During physical field interpolation, since some DrivAerNet++ samples are simulated using only half of the geometry, we map each sampled point to its symmetric counterpart when necessary. For the U-Net and GNN surrogate models used in guided diffusion sampling and topology-preserving optimization, we employ the drag coefficient values provided by the DrivAerNet++ dataset as ground truth supervision during training.

D Implementation details.

Our framework consists of three key components: the Physics–Geometry VAE (PG-VAE), Objective-Guided Diffusion, and Topology-Preserving Refinement. Below, we provide detailed implementation descriptions for each component.

PG-VAE. The PG-VAE serves to compress both the design geometry and the corresponding physical field into a unified latent representation. We sample $N_g = N_p = 50,000$ points for the geometry and physical field branches, respectively. The encoder consists of one cross-attention layer and eight self-attention layers, each with 12 attention heads and an embedding dimension of $d_z = 64$. We use $r = 64$ for learnable tokens, and each with a channel dimension of $d_e = 768$, to enhance representation expressiveness. The latent code dimension is set to $d_z = 32$. The decoder architecture consists of one self-attention layer followed by five ResNet blocks [69], which upsample the latent vector into a triplane representation with resolution $R = 256$ and channel dimension $d_t = 64$. The output triplane is then queried using a mapping network composed of five fully connected layers with a hidden size of 32 per branch. We adopt a semi-continuous occupancy formulation [60] and supervise both occupancy and physical field predictions using 50,000 sampled points within the normalized unit cube. We optimize the VAE using a combination of three loss terms: binary cross-entropy loss ($\lambda_{\text{BCE}} = 10^{-3}$), mean squared error for field regression ($\lambda_{\text{MSE}} = 10^{-5}$), and KL divergence ($\lambda_{\text{KL}} = 10^{-6}$). Training is performed using the AdamW optimizer [71] with a learning rate of 1×10^{-4} , batch size 8 per GPU, for 100,000 steps. We use four NVIDIA RTX A6000 GPUs to train the model.

Objective-Guided Diffusion. To explore the latent design space efficiently, we employ a latent-space diffusion model composed of 10 DiT blocks [70], each containing 16 attention heads with a head dimension of 72. The diffusion process includes 1,000 denoising steps. During inference, an auxiliary U-Net surrogate network is used to predict the task objective directly from the latent code z , thereby guiding the sampling process toward optimal designs. The diffusion model is trained using a learning rate of 5×10^{-5} , batch size of 4 per GPU, for 300,000 steps with the AdamW optimizer. We use four NVIDIA RTX A6000 GPUs to train the diffusion model.

Topology-Preserving Refinement. To refine the initial design candidates while maintaining mesh topology, we apply a Free-Form Deformation (FFD) grid with $20 \times 6 \times 6$ control points along the x, y, and z axes, respectively. The deformation is guided by a surrogate model based on Mesh-GraphNet [30], which comprises 8 message-passing blocks and operates on the surface mesh. The

MeshGraphNet is trained to predict the drag force from a deformed mesh, serving as a differentiable objective function during refinement. This model is trained with a learning rate of 1×10^{-5} , batch size of 8 per GPU, for 100,000 steps, using AdamW as the optimizer. We use two NVIDIA RTX A6000 GPUs to train the MeshGraphNet.

E Evaluation details.

In our experiments, we evaluate the design candidates using four metrics: predicted drag force (Pred-Drag), simulated drag force (Sim-Drag), novelty, and coverage.

Pred-Drag. We use the pretrained surrogate model to estimate the drag force of each candidate mesh. Given the mesh of designed candidates M^* , our surrogate model directly predict the objective drag force $\hat{\mathcal{J}}$ which can be formalized as:

$$\hat{\mathcal{J}} = \mathcal{F}_{\text{surrogate}}(M^*), \quad (12)$$

where $\mathcal{F}_{\text{surrogate}}$ denotes the learned mapping from 3D mesh geometry to the predicted drag coefficient. For our surrogate model, we adopt a MeshGraphNet [30] with 8 message passing blocks as the surrogate model. Unlike the model used in our topology-preserving refinement stage, this predictor operates solely on geometry, without requiring the associated physical field. To train the model, we use the entire DrivAerNet++ [72] dataset. Given that different representations may produce varying topological structures, we apply remeshing and simplification to all candidates for fair comparison.

Sim-Drag. To obtain an unbiased evaluation of the generated designs, we perform high-fidelity Computational Fluid Dynamics (CFD) simulations and compute the corresponding drag coefficients. Following DrivAerNet++ [72], we employ the OpenFOAM@V11 [79] to conduct steady-state incompressible simulation using the $k - \omega$ SST turbulence model, based on Menter’s formulation [80]. We performed a series of quality checks to ensure the generated geometries were simulation-ready and properly aligned within the CFD domain. During simulation, considering the computation cost, we set the maximum local cells to 10 million and the maximum global cells to 50 million in snappyHexMesh. The simulation iterates for 1000s, and we use the final 30% simulation data to calculate the average drag coefficient. The hyperparameters of our simulation are provided in Table 8.

Novelty. To quantitatively assess how different the generated designs are from the training data, we measure the novelty of each candidate. Specifically, novelty is computed as the average distance from each generated design to its nearest neighbor in the training set, reflecting how distinct the generated designs are from existing ones. Let $\{g_i\}_{i=1}^{N_g}$ denote the set of generated designs and $\{t_j\}_{j=1}^{N_t}$ denote the set of training designs in the feature space. The novelty is defined as:

$$\text{Novelty} = \frac{1}{N_g} \sum_{i=1}^{N_g} \min_j d(g_i, t_j), \quad (13)$$

where $d(\cdot, \cdot)$ denotes the distance between feature embeddings, computed using the pretrained PointNet encoder [75].

Coverage. The coverage metric (also known as recall) evaluates how well the generated designs cover the training distribution by measuring, for each training sample, the distance to its nearest generated design (using a k-nearest neighbor lookup) and reporting the fraction of training examples that fall within a predefined threshold. Let $\{g_i\}_{i=1}^{N_g}$ denote the set of generated designs and $\{t_j\}_{j=1}^{N_t}$ denote the set of training designs in the feature space. The coverage is defined as:

$$\text{Coverage} = \frac{1}{N_t} \sum_{j=1}^{N_t} \mathbf{1}[\min_i d(t_j, g_i) \leq \tau] \quad (14)$$

where $d(\cdot, \cdot)$ is a distance metric, τ is a predefined threshold, and $\mathbf{1}[\cdot]$ is the indicator function that equals 1 if the condition is true and 0 otherwise.

F Broader Impacts

Academic Impact. 3DID’s methodology, which enables direct navigation through 3D physics-geometry space, simplifies the 3D inverse design process. With the unified physics-geometry representation, the computation gap between 3D and lower-dimensional inverse design is narrowed, allowing researchers to focus more on exploring cutting-edge inverse design strategies rather than being constrained by computational limitations. With the two-stage optimization strategy, our method balances between exploration and validity, offering researchers an effective approach for inverse design involving 3D geometry.

Social Impact. The proposed 3D Inverse Design (3DID) framework extends the scope of geometry-driven design by enabling direct optimization of full 3D structures from scratch. By combining unified physics-geometry representations with physics-aware optimization, our method opens the door to more efficient, automated design workflows in fields such as aerospace engineering, biomedicine, additive manufacturing, and nanophotonics. In particular, 3DID can be applied to complex design tasks that traditionally rely on expert-crafted initial geometries and time-consuming simulation-based evaluations. In mechanical engineering, it can be used to optimize structural components for strength, weight, and thermal performance without manual trial-and-error. In the medical field, 3DID enables the fabrication of patient-specific implants by automatically generating geometries tailored to individual physiological and functional requirements.

G License

The code will be publicly accessible. We use standard licenses from the community. We include the following licenses for the codes, datasets, and models we used in this paper.

1. **Dataset**
 - DrivAerNet++ [72]: CC BY-NC 4.0
2. **Codes**
 - NVIDIA PhysicsNeMo: Apache License 2.0
3. **Evaluation**
 - OpenFOAM [79]: GNU General Public License

Table 5: **Hyperparameters for Voxel-VAE**

Hyperparameter name	Value
Hyperparameters for Voxel-VAE architecture:	
Input shape	[8, 256, 256, 256]
Output shape	[8, 256, 256, 256]
Number of 3D convolution layer	5
Dimension of latent z_{voxel}	512
Number of 3D transposed convolutional layer	5
Number of MLPs in drag predictor	5
Batch size	8
Dimension of encoder	(1, 32, 64, 128, 256, 512)
Dimension of voxel decoder	(512, 256, 128, 64, 32, 1)
Dimension of drag predictor	(512, 256, 128, 64, 32, 1)
Hyperparameters for Voxel-VAE training:	
Optimizer	AdamW
Learning rate	$1e - 4$
Learning steps	100K
Learning rate adjustment strategy	Cosine
Warm-up steps	5K
$\mathcal{L}_{\text{recon}}$ weight	10^{-3}
\mathcal{L}_{KL} weight	10^{-4}
$\mathcal{L}_{\text{drag}}$ weight	10^{-3}

Table 6: **Hyperparameters for Voxel-PCA-VAE**

Hyperparameter name	Value
Hyperparameters for Voxel-PCA-VAE architecture:	
PCA output dimension	400
Number of MLP layers in encoder	4
Dimension of latent $z_{\text{voxel-pca}}$	64
Number of MLP layers in decoder	4
Number of MLPs in drag predictor	2
Batch size	32
Dimension of encoder	(400, 256, 128, 64, 64)
Dimension of PCA decoder	(64, 64, 128, 256, 400)
Dimension of drag predictor	(64, 32, 1)
Hyperparameters for Voxel-PCA-VAE training:	
Optimizer	AdamW
Learning rate	$5e - 4$
Learning steps	100K
Learning rate adjustment strategy	Cosine
Warm-up steps	5K
$\mathcal{L}_{\text{recon}}$ weight	10^{-2}
\mathcal{L}_{KL} weight	10^{-4}
$\mathcal{L}_{\text{drag}}$ weight	10^{-3}

Table 7: **Hyperparameters for TripNet VAE**

Hyperparameter name	Value
Hyperparameters for TripNet-VAE training:	
Batch size	8
Optimizer	AdamW
Learning rate	$1e - 4$
Learning steps	100K
Learning rate adjustment strategy	Cosine
Warm-up steps	5K
\mathcal{L}_{BCE} weight	10^{-3}
\mathcal{L}_{KL} weight	10^{-6}

Table 8: CFD Simulation Parameters for OpenFOAM

Parameter name	Value
Solver Configuration:	
OpenFOAM version	v11
Solver	incompressibleFluid
Algorithm	SIMPLE
Turbulence model	k- ω -SST
Simulation type	Steady-state RANS
Flow Conditions:	
Flow velocity (u_∞)	30 m/s
Kinematic viscosity (ν)	1.56×10^{-5} m ² /s
Air density (ρ)	1.184 kg/m ³
Turbulent kinetic energy (k)	0.375 m ² /s ²
Specific dissipation rate (ω)	1.78 s ⁻¹
Computational Domain:	
Domain dimensions	44×8×6.4 m
Inlet distance	12 m upstream
Outlet distance	32 m downstream
Solver Tolerances:	
Pressure absolute tolerance	1×10^{-6}
Pressure relative tolerance	3×10^{-2}
Velocity absolute tolerance	1×10^{-8}
Velocity relative tolerance	5×10^{-3}
Turbulence absolute tolerance	1×10^{-8}
Turbulence relative tolerance	1×10^{-3}
Potential solver absolute tolerance	1×10^{-7}
Potential solver relative tolerance	1×10^{-2}
Mesh Refinement:	
Surface refinement level	3-4
Feature refinement level	4
Regional refinement level	2
Wake refinement level	2
Boundary layers	5 layers
Layer expansion ratio	1.2
Final layer thickness	0.5
Force Calculation:	
Reference length (l_{ref})	4.777 m
Reference area (A_{ref})	2.0 m ²
Reference center	(0, 0, 0)
Drag direction	(1, 0, 0)
Lift direction	(0, 0, 1)
Simulation Control:	
End time	1000 s
Time step	1 s
Write interval	100 steps
Force coeffs write interval	10 steps